

JWST Confirmation of a Runaway Supermassive Black Hole via its Supersonic Bow Shock

PIETER VAN DOKKUM,¹ CONNOR JENNINGS,¹ IMAD PASHA,^{1,2} CHARLIE CONROY,³ ISH KAUL,⁴ ROBERTO ABRAHAM,^{5,2}
SHANY DANIELI,⁶ AARON J. ROMANOWSKY,^{7,8} AND GRANT TREMBLAY³

¹*Astronomy Department, Yale University, 219 Prospect St, New Haven, CT 06511, USA*

²*Dragonfly Focused Research Organization, 150 Washington Avenue, Suite 201, Santa Fe, NM 87501, USA*

³*Harvard-Smithsonian Center for Astrophysics, 60 Garden Street, Cambridge, MA, USA*

⁴*Department of Physics, University of California, Santa Barbara, CA 93106, USA*

⁵*Department of Astronomy & Astrophysics, University of Toronto, 50 St. George Street, Toronto, ON M5S 3H4, Canada*

⁶*School of Physics and Astronomy, Tel Aviv University, Tel Aviv 69978, Israel*

⁷*Department of Physics and Astronomy, San José State University, San Jose, CA 95192, USA*

⁸*Department of Astronomy and Astrophysics, University of California Santa Cruz, 1156 High Street, Santa Cruz, CA 95064, USA*

ABSTRACT

We present JWST/NIRSpec IFU observations of a candidate runaway supermassive black hole at the tip of a 62 kpc-long linear feature at $z = 0.96$. The JWST data show a sharp kinematic discontinuity at the tip, with a radial velocity change of $\approx 600 \text{ km s}^{-1}$ across $0''.1$ (1 kpc). The velocity gradient, together with the projected post-shock flow velocity of $\approx 300 \text{ km s}^{-1}$, is well described by a simple shock-compression model of a supersonic object, with a velocity of $v_{\bullet} = 954^{+110}_{-126} \text{ km s}^{-1}$ and an inclination $i = 29^{+6}_{-3} \text{ deg}$. The previously puzzling kinematics along the linear feature, with the observed radial velocity decreasing from $\approx 300 \text{ km s}^{-1}$ near the tip to $\approx 100 \text{ km s}^{-1}$ closer to the former host galaxy, are naturally explained as gradual downstream mixing of shocked gas with the circumgalactic medium through turbulent entrainment. The interpretation is further supported by the morphology of the gas at the tip of the wake and an analysis of the [O III]/H α , [N II]/H α , [S II]/H α , and [S III]/[S II] line ratios. The line ratios are consistent with fast radiative shocks and rapid cooling, with best-fit shock velocities that are in good agreement with expectations from the black hole velocity and the shock geometry. Energy conservation over the lifetime of the wake suggests a SMBH mass of $M_{\bullet} \gtrsim 10^7 M_{\odot}$. These results confirm that the wake is powered by a supersonic runaway supermassive black hole, a long-predicted consequence of gravitational-wave recoil or multi-body ejection from galactic nuclei.

1. INTRODUCTION

The occasional escape of supermassive black holes (SMBHs) from their host galaxies is a long-standing prediction of theoretical studies. Velocity kicks can be imparted through two distinct channels: a slingshot resulting from a three-body interaction (Saslaw et al. 1974; Volonteri et al. 2003; Hoffman & Loeb 2007) or gravitational wave recoil following a BH-BH merger (Bekenstein 1973; Campanelli et al. 2007). Both channels occur naturally as a result of galaxy – galaxy mergers, as the black holes of the ancestor galaxies end up in the center of the descendant. If the imparted velocity exceeds the escape velocity, the SMBH will leave the host and continue to travel through intergalactic space (see, e.g., Saslaw et al. 1974; Hoffman & Loeb 2007; Lousto et al. 2012; Ricarte et al. 2021).

At present, no such “runaway” SMBHs have been confirmed, although there are several promising candidates. Most of these are double or triple active galactic nuclei (AGNs), or AGNs that are displaced from the center of their host galaxy (e.g., Magain et al. 2005; Komossa et al. 2008;

Civano et al. 2010; Robinson et al. 2010; Chiaberge et al. 2017; Liu et al. 2025). The interpretation of these systems is often ambiguous; in particular, it is difficult to distinguish ongoing mergers from ejections (see, e.g., Merritt et al. 2006). A special case is the ∞ galaxy (van Dokkum et al. 2025a), also known as the Cosmic Owl (Li et al. 2025). This object has two nuclei and three active SMBHs, with one of the black holes embedded in a gas cloud in between the two nuclei. This third SMBH might have escaped from one of the nuclei in a three-body interaction, but in van Dokkum et al. (2025a) and its JWST IFU follow-up van Dokkum et al. (2025b) it is argued that it is more likely that it formed in-situ through a direct collapse.

Arguably the best candidate for a SMBH that has completely escaped from its former host is a remarkable linear feature that was serendipitously discovered in an HST image (van Dokkum et al. 2023, hereafter Paper I). The linear feature, here dubbed RBH-1, extends 62 kpc from a $z = 0.96$ galaxy. Keck/LRIS spectra show line emission along the entire extent of the feature, culminating in a bright knot of

[O III] emission at the tip. In Paper I we interpreted the object as the wake of a runaway SMBH, with the tip the shock front where the SMBH encounters the circumgalactic medium (CGM). Theoretical support for this interpretation came from predictions of [Saslaw & De Young \(1972\)](#) and [de la Fuente Marcos & de la Fuente Marcos \(2008\)](#), who studied the interaction of runaway SMBHs with the surrounding gas.

Following the publication of Paper I, [Ogiya & Nagai \(2024\)](#) showed that several of the observed features of RBH-1 are indeed reproduced in a hydrodynamical simulation of the gravitational interaction between the CGM and a passing SMBH. However, others have proposed alternative interpretations: [Sánchez Almeida et al. \(2023\)](#) suggest that the linear feature is an edge-on, bulgeless galaxy, and [Chen et al. \(2023\)](#) interpret the object as a partially-shredded galaxy with a SMBH at one end. The main limitation of the runaway SMBH interpretation was that it rested on circumstantial evidence: in Paper I we did not directly demonstrate the presence of a high velocity object. Here we present JWST/NIRSpec observations that provide confirmation of a supersonic massive perturber at the tip of RBH-1.

2. DATA

The key new data are JWST NIRSpec IFU observations. We also briefly describe new HST imaging data and – in § 6.2.1 and § C – re-analyze the Keck/LRIS data of Paper I.

2.1. Deep HST WFC3/UVIS Imaging

The field of RBH-1 was observed with HST WFC3/UVIS in Cycle 30, in program HST-GO-17301 (PI: van Dokkum). Two long pass filters were used, F200LP and F350LP, with six orbits in each of the filters. Three exposures were obtained in each orbit, with small offsets to facilitate bad pixel removal and improve subpixel sampling. The total exposure time is 14,976 s in F200LP and 14,922 s in F350LP.

The data were reduced in the following way. In the UVIS longpass filters the background shows large scale gradients, caused by the difficulty of flat fielding these very broad filters (see [Mack et al. 2016](#)). We used a low order polynomial fit to remove the background for each individual chip in each exposure. The F200LP and F350LP exposures were then drizzled to an $0''.04 \text{ pix}^{-1}$ grid at an orientation of 122° . This orientation places the linear feature along the x -axis with the galaxy at left and the tip at right. The difference between the filters, $\text{LP}_{\text{diff}} = \text{F200LP} - 1.22 \times \text{F350LP}$, creates a UV pass-band from $\sim 200 \text{ nm}$ to $\sim 350 \text{ nm}$. The sum of the filters, $\text{LP}_{\text{sum}} = \text{F200LP} + \text{F350LP}$, produces a 12-orbit deep “white light” optical image.

The LP_{sum} image of the linear feature and the associated galaxy is shown in Fig. 1. The intensity along the feature is shown in the panel below the image, derived from summing the central 8 rows ($0''.32$). The deep data show that there is

continuous emission all the way from the galaxy to the tip of the feature, including in the apparent gap between the streak in the original ACS-imaging and the galaxy (something we also noted in VLT B band data; see [van Dokkum 2023](#)). Furthermore, the data confirm that the feature does not extend beyond the tip at $r \approx 62 \text{ kpc}$. The drop is a factor of > 40 at 95 % confidence, which is difficult to reconcile with the expected exponential decline of an edge-on disk or the surface brightness profile of a tidal feature ([Sánchez Almeida et al. 2023](#); [Chen et al. 2023](#)).

The data do not show any emission on the opposite side of the galaxy, in either LP_{sum} or LP_{diff} , in conflict with a low significance CFHT u -band detection of a counter-wake in Paper I. One of the goals of the UVIS observations was to assess whether this apparent counter-wake actually exists, and we conclude that it does not (see also [Montes et al. 2024](#)).

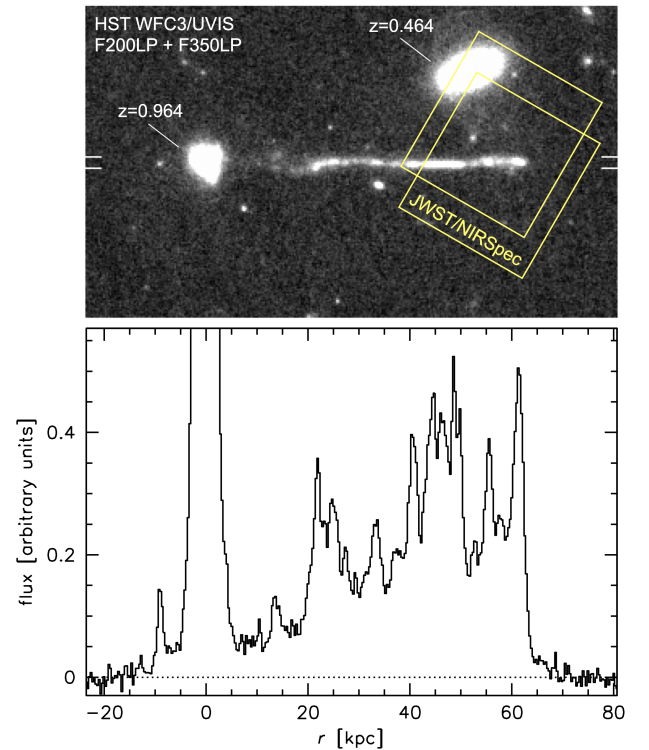


Figure 1. *Top:* HST/WFC3 UVIS imaging of the candidate $z = 0.96$ runaway black hole wake RBH-1. The displayed image spans $13''.2 \times 7''.7$. It is the sum of two long pass filters, F200LP and F350LP, with a combined integration time of 29,898 s. The two JWST NIRSpec pointings are indicated in yellow. *Bottom:* summed flux profile along the feature. There is continuous emission all the way from the galaxy to the tip at $r \approx 62 \text{ kpc}$, followed by a sudden drop of a factor of > 40 . The profile does not resemble the exponential fall-off expected for an edge-on spiral galaxy (an interpretation that was proposed by [Sánchez Almeida et al. 2023](#)).

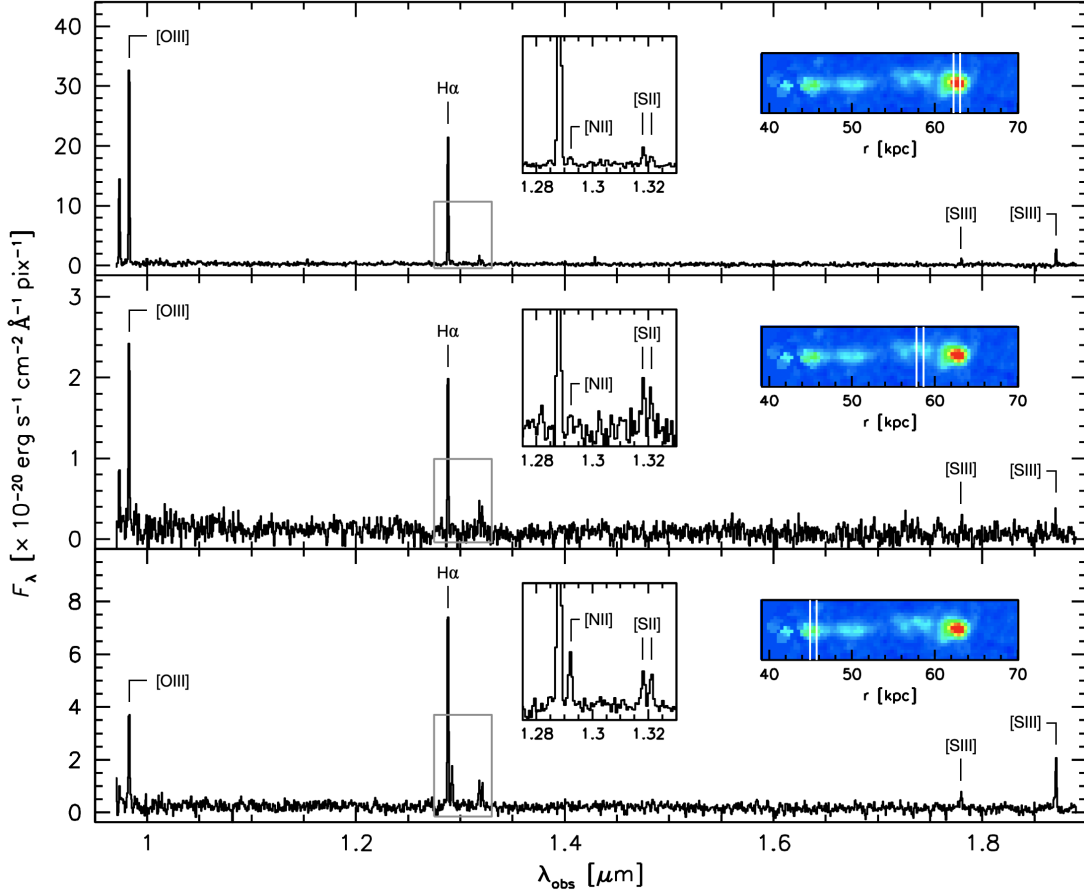


Figure 2. Overview of the NIRSpec IFU data. Insets show a map of the redshifted [O III] emission, with three characteristic locations indicated by vertical lines. The main panels show the spectra at those locations. There is a distinct, very bright knot at the tip of RBH-1, with a high [O III]/H α ratio. This ratio decreases gradually behind the tip, while the [N II]/H α and [S II]/H α ratios increase. In all panels [O III] and H α are the strongest lines; these are used for the dynamical analysis in § 4.

2.2. JWST NIRSpec Observations

2.2.1. Observing Program and Data Reduction

We obtained spatially-resolved spectroscopy of the tip of RBH-1 with the JWST NIRSpec Integral Field Unit (IFU) on July 24 2024, in Cycle 2 program JWST-GO-3149 (PI: van Dokkum). The observations are divided over two target positions, symmetrically placed on each side of the linear feature 0.''5 downstream from the tip (see Fig. 1). The 0.''1 spaxels of the IFU undersample the point spread function (PSF); at each of the two target positions a 4-point dither pattern samples the PSF on a 0.''05 grid. The G140M/F100LP grating and filter combination gives wavelength coverage from $0.97\ \mu\text{m}$ – $1.89\ \mu\text{m}$, corresponding to $0.49\ \mu\text{m}$ – $0.96\ \mu\text{m}$ in the restframe. The spectra do not include H β but cover [O III], H α , [N II], [S II], and [S III], along with fainter lines. The spectra are sampled on a grid with a $6.4\ \text{\AA}$ spacing, corresponding to $193\ \text{km s}^{-1}$ at [O III] and $147\ \text{km s}^{-1}$ at H α . The total integration time was 3549 s for each pointing, for a total of 7089 s.

The data were reduced with the TEMPLATES pipeline (Rigby et al. 2023), built on the JWST Science Calibration Pipeline (Bushouse et al. 2025) (v1.18.0). The method follows that of van Dokkum et al. (2025b); here we summarize briefly. Uncalibrated exposures from MAST (JWST SDP v2025_2) were processed through the stage 1 detector-level pipeline, followed by $1/f$ noise correction with NSClean (Rauscher 2024). Stage 2 spectroscopic calibration was run, and cosmic rays were identified as outlier spaxels. The NRS1 data from all exposures and all dithers were then combined, with no background subtraction. Taking advantage of the subpixel sampling of the dither pattern, the data were combined onto a 0.''05 grid, corresponding to the angular scale that is sampled by the dither pattern.

These steps were performed for each of the two target positions. To remove background structures and detector artifacts, we subtracted the two pointings from one another. A copy of the difference cube was shifted by the distance between the two pointings, multiplied by -1 , and added to the original difference cube. This procedure results in a positive

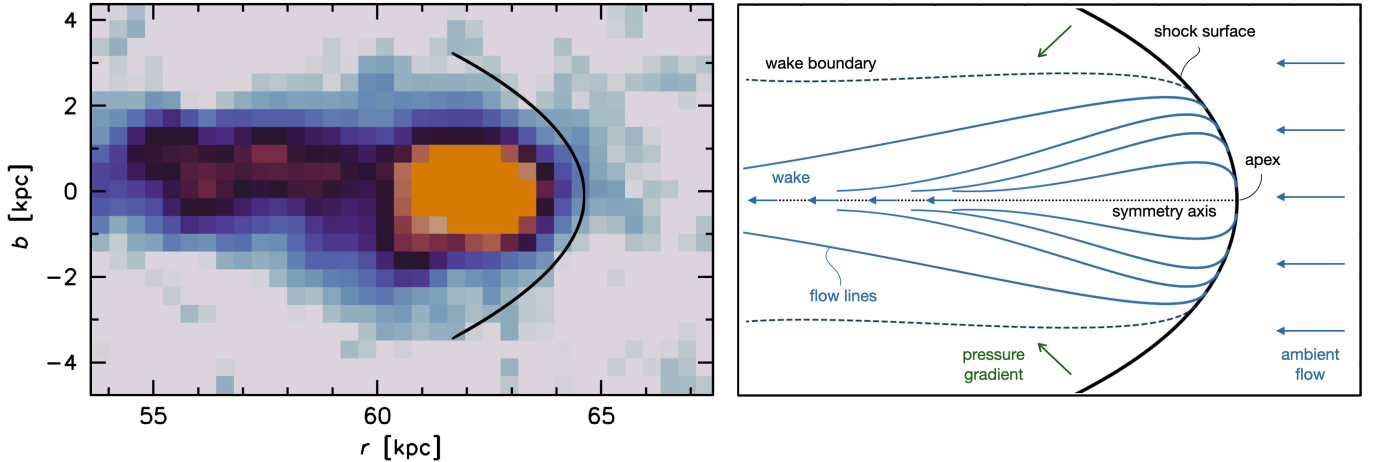


Figure 3. *Left:* Summed [O III] + $H\alpha$ line emission at the tip of the linear feature. The tip is clearly resolved, and resembles a classic bow shock with a thin turbulent wake behind it. The thick black line is a restricted parabolic fit to a faint isophote at $63 \leq r \leq 65$ kpc. *Right:* Illustration of a bow shock, at approximately the same scale. Upon encountering the shock gas flows tangentially along the shock surface. The low pressure behind the shock causes flow lines to bend toward the symmetry axis, creating a narrow wake.

summed version of the linear feature in the center of the field, flanked by negative versions from each of the two pointings.

2.2.2. Qualitative Description of the Data

An overview of the reduced data is shown in Fig. 2. The insets show a map of the [O III] emission, created by summing the three wavelength bins with strong [O III] emission. There is significant structure in the feature. The tip is distinct from the rest of RBH-1 and very bright in [O III]. There is no detected emission upstream from the tip. While the tip is compact, it is spatially resolved (as anticipated in paper I). Behind the tip, at $55 \text{ kpc} \lesssim r \lesssim 60 \text{ kpc}$, is a turbulent region with several knots. Further downstream the wake narrows and there are more concentrations.

Three spectra are shown, for the tip, the turbulent region just behind it, and an area further downstream. The strongest redshifted emission lines are [O III] $\lambda 5007$, $H\alpha$, [N II] $\lambda 6584$, the [S II] $\lambda\lambda 6716, 6731$ doublet, and the [S III] $\lambda\lambda 9069, 9532$ doublet. There are striking differences between the spectra. At the tip, the strongest line is [O III], [N II] is barely detected, and [S II] is faint compared to [S III]. Behind the tip the [O III]/ $H\alpha$ ratio decreases and [S II]/ $H\alpha$ ratio increases. The [N II] line remains weak, until we are quite far downstream. We will return to this in § 5.

3. MORPHOLOGICAL EVIDENCE FOR A BOW SHOCK WITH A TURBULENT WAKE

We begin by analyzing the ionized gas morphology of the tip region in the JWST data cube. In paper I we predicted that the shock should be spatially-resolved at $\sim 0''.1$ resolution: the [O III] surface brightness of fast radiative shock is limited by the incoming energy flux, and the models of Dopita & Sutherland (1996) imply a total area of the shock front of

$\sim 0.2n^{-1} \text{ kpc}^2$ for the observed [O III] luminosity (with $n \sim 10^{-3}$ the density of the CGM).

The tip of the wake is shown in Fig. 3. To create this image we summed the [O III] $\lambda 5007$ and $H\alpha$ maps in order to maximize the S/N ratio of faint emission. As expected the tip region is not a point source but clearly resolved, both in the direction away from the galaxy (r) and in the perpendicular (b) direction. The faint contours flare out from the tip to reach a total width of $\Delta b \approx 6 \text{ kpc}$ at $r \approx 61 \text{ kpc}$ and then taper downstream. The emission breaks up into several distinct knots at $55 \text{ kpc} \lesssim r \lesssim 60 \text{ kpc}$.

This is the classic morphology of a bow shock with a turbulent wake, as illustrated in the right panel of Fig. 3. The ambient flow, here the CGM, is decelerated in the direction normal to the shock and deflected along the shock surface. The low pressure behind the shock front then bends the flow lines toward the symmetry axis, leading to tapering and a narrow wake (see, e.g., Wilkin 1996; Bucciantini 2002; Tarango-Yong & Henney 2018; Meyer et al. 2017). Well-known examples with similar morphology are the bow shocks associated with Mira (Martin et al. 2007) and the Herbig-Haro objects HH 1 (Bally et al. 2002) and HH 34 (Reipurth et al. 2002).

It is not very meaningful to quantify the width of the shock with traditional measures such as the FWHM: the emission lines do not peak in the shock front itself but in the compression and cooling zone behind it, as this is where the temperature has decreased to 10^{4-5} K and the density is highest. Flux-weighted quantities therefore measure the extent of the cooling zone, not the shock front. Instead, we characterize the geometry by fitting a parabola to an outer contour. The local radius of curvature at the apex, R_c , is relatively robust against thresholds or the flux distribution inside the shock. Once

R_c is known, the shock radius downstream follows from the parabolic fit, using $R_{\text{phot}}(\Delta r_{\text{apex}}) = \sqrt{2R_c \Delta r_{\text{apex}}}$ with Δr_{apex} the distance from the apex.

The thick line in Fig. 3 shows the best-fitting parabola, with the fit restricted to a faint contour (1σ above the background) and a radial range $63 \text{ kpc} \leq r \leq 65 \text{ kpc}$. The apex location of the parabola $r_{\text{apex}} \approx 64.6 \text{ kpc}$ and the radius of curvature $R_c \approx 1.8 \text{ kpc}$. The associated stand-off scale is $R_0 \approx \frac{2}{3}R_c \approx 1.2 \text{ kpc}$ (Wilkin 1996). The shock extends approximately 4 kpc behind the apex and its total area is $\sim 80 \text{ kpc}^2$, in reasonably good agreement with our [O III] luminosity-based estimate in Paper I.

4. BOW SHOCK KINEMATICS

4.1. Qualitative Expectations

Bow shocks produce distinct signatures in the line-of-sight (LOS) kinematics that can be used to infer the orientation and velocity of the shock. As discussed above and shown in Fig. 3, gas initially flows along the limbs of the bow and then bends towards the symmetry axis to form the wake. If the shock is viewed exactly side-on ($i = 0^\circ$ with respect to the plane of the sky), there will be no LOS velocity in the wake region: all the motion in the wake is in the plane of the sky. The velocities in the limbs of the bow are strongly redshifted and blueshifted, as gas on the near limb is coming toward the observer and gas on the far limb is moving away from the observer. The net effect is a broad LOS velocity distribution at the tip and a narrow distribution further downstream, with a mean velocity of ~ 0 everywhere. If the shock is viewed exactly from the front ($i = 90^\circ$) the LOS velocity will be dominated by the wake, as the gas on the limbs flows mainly in the plane of the sky. The wake velocity will be blueshifted with respect to the ambient medium if the object is coming towards the observer and redshifted if it is moving away from the observer.

More commonly the shock will be tilted at an intermediate angle. This situation is illustrated in Fig. 4, where we show a 3D rendering of a flow surface that is tilted toward the observer at an angle of 50° . With respect to the LOS velocity in the wake, gas on the near limb is blueshifted and gas on the far limb is redshifted. Furthermore, the blueshifted limb is projected at a different location than the redshifted limb: going downstream from the apex, the gas is first redshifted and then blueshifted. As a result, bow shocks often produce a tilted locus in position-velocity diagrams for intermediate viewing angles (see, e.g., Hartigan et al. 1987; Indebetouw & Noriega-Crespo 1995; López-Martín et al. 2002).

4.2. A Steep Velocity Gradient at the Tip of the Wake

Remarkably, inspection of the data cubes shows clear evidence for such a gradient at the tip of RBH-1: the centroid of emission moves systematically upstream with increasing

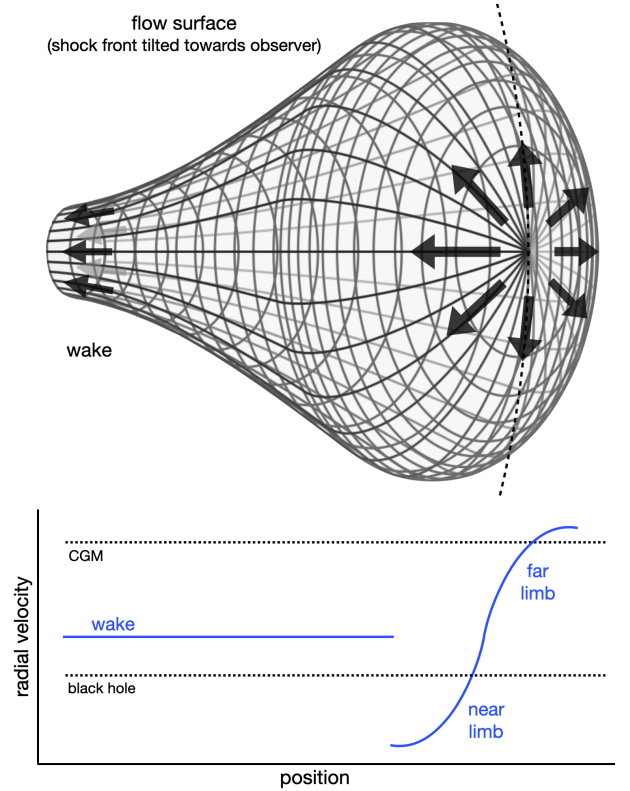


Figure 4. Illustration of a flow surface for a shock that is projected at an intermediate angle (50°) toward the observer. Gas on the near limb is blueshifted and gas on the far limb is redshifted with respect to the wake velocity. The blueshifted gas is projected further downstream than the redshifted gas, leading to a velocity gradient.

wavelength. This is demonstrated in the central panel of Fig. 5, where we show wavelength channels around the redshifted [O III] $\lambda 5007$ and $H\alpha$ lines. By collapsing the flux in these maps vertically, that is, perpendicular to the wake direction, we obtain position-velocity diagrams, shown in the left and right panels of Fig. 5. Following the convention of Paper I we calculate velocities with respect to the redshift of the galaxy.

We find a well-defined and extremely steep velocity gradient in both [O III] and $H\alpha$, going from about -600 km s^{-1} to $+50 \text{ km s}^{-1}$ across $\sim 1 \text{ kpc}$ ($0''.1$). The trends are quantified with a quadratic interpolation to find the location of the centroid in each velocity channel (white data points). We note that the *peak* of emission is always in the central channels, that is, near $\sim -300 \text{ km s}^{-1}$. This is consistent with the Keck spectroscopy of Paper I, which shows a plateau at that approximate velocity beyond $r \gtrsim 50 \text{ kpc}$.

We thus find that the observed kinematics at the tip of RBH-1 are qualitatively consistent with expectations for a strong supersonic bow shock. Furthermore, in Appendix A we show that the observed gradient can *not* be produced by the gravitational influence of a black hole, as the implied black hole mass would be orders of magnitude higher than

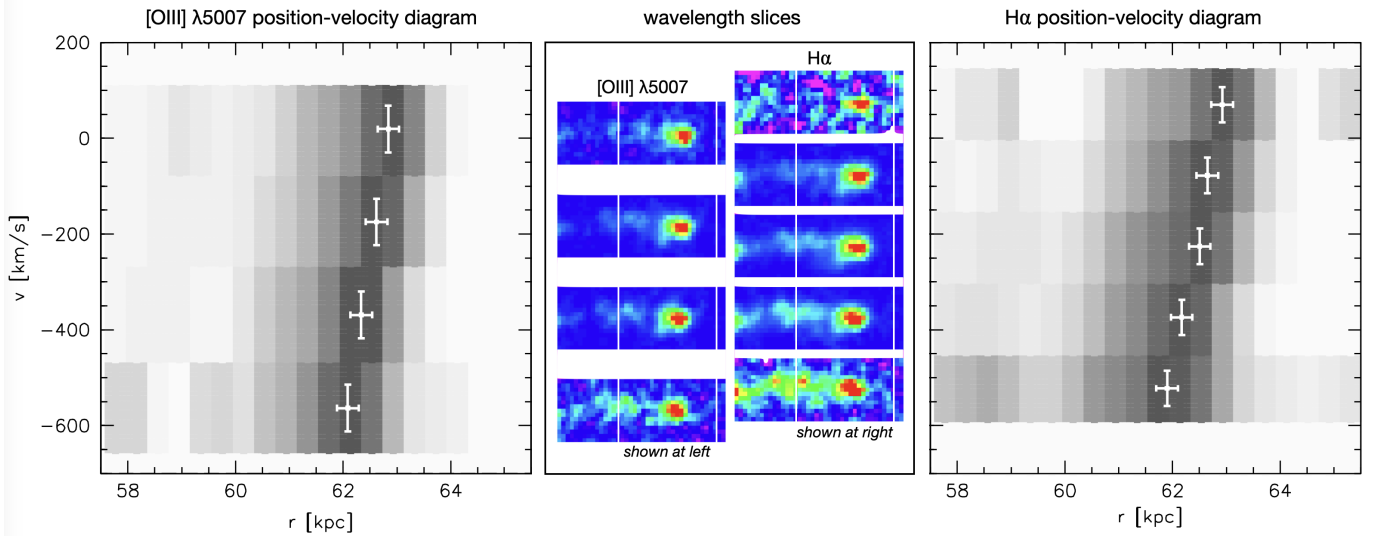


Figure 5. *Middle:* Wavelength slices through the data cube, near the wavelength of the redshifted [O III] $\lambda 5007$ line (left) and $H\alpha$ (right). Fluxes have been scaled to the peak in each slice. There is a striking pattern, with the emission near the tip systematically shifting further upstream for higher velocities. *Left and right:* Position-velocity diagrams for the regions in between the white lines, obtained by averaging the flux in the direction perpendicular to the wake. These diagrams show an unambiguous gradient of $\sim 600 \text{ km s}^{-1}$ over $\sim 1 \text{ kpc}$. The gradient is quantified by the white data points.

is reasonable. In the following, we develop a quantitative bow shock model to determine key parameters such as the velocity of the black hole and the inclination of the wake.

4.3. Quantitative Bow Shock Model

4.3.1. Velocity Components

The model is a simplified version of the full treatment offered by Wilkin (1996) and others, geared toward fitting the velocity gradient. The geometry and relevant gas flow directions are illustrated in Fig. 6. While the gas flow is continuous, we separate it into two distinct components: the tangential flow on the shock surface and the flow in the post-shock wake. The tangential flow dominates near the apex, and is to good approximation

$$v_t(\theta) \approx v_\bullet \sin \theta, \quad (1)$$

with θ the local shock obliquity. This is the angle between the shell normal and the black hole direction of motion, as indicated in Fig. 6: $\theta = 0^\circ$ at the apex and increases downstream as the shock surface flares.

The flow in the wake is dominated by the velocity component that is normal to the shock surface. The shock reduces this normal component by the compression factor χ , such that

$$v_{\text{wake}} \approx v_n \approx \frac{v_\bullet}{\chi}. \quad (2)$$

The compression factor satisfies $\chi \leq 4$ for a strong adiabatic shock with $\gamma = 5/3$ (e.g., Draine 2011), and in typical ISM conditions the immediate compression is typically $\chi = 3\text{--}3.5$ (e.g., Anderson 2003; Draine & McKee 1993; Draine 2011). We adopt $\chi = 3$ in the main analysis.

These expressions are in the rest-frame of the black hole, that is, the flow is seen as coming towards a static shock. However, the observed kinematics are not in the black hole rest-frame but in the rest-frame of the CGM (or, more precisely, that of the former host galaxy), and also projected along the line of sight. Adding the black hole velocity $+v_\bullet$ and tilting the symmetry axis by the inclination i (the angle out of the sky plane, toward the observer) gives the following expression for the normal component:

$$v_{\text{LOS, wake}} \approx v_\bullet \left(1 - \frac{1}{\chi}\right) \sin i. \quad (3)$$

The entire structure acquires this baseline in the BH \rightarrow CGM translation.

Next, we project the tangential velocity along the line of sight. For simplicity we determine the line of sight velocity for a circular cross section at a fixed obliquity θ . The azimuth around the axis of the cross section is denoted by ϕ , with the convention that $\phi = 0$ at the far limb (back, away from the observer), $\phi = \pi$ at the near limb (front, toward the observer), and $\phi = \pm\pi/2$ at the sides. Projecting the tangential direction to the LOS gives the near–far (antisymmetric) contribution

$$\Delta v_{\text{LOS}}(\phi; \theta) \approx v_\bullet \sin \theta \cos \theta \cos i \cos \phi. \quad (4)$$

Hence the observed LOS velocity in the region near the apex is

$$v_{\text{LOS}}(\phi; \theta) \approx v_{\text{LOS, wake}} \pm \Delta v_{\text{LOS}}, \quad (5)$$

with the sign set by the local $\cos \phi$ (blueshifted on the near limb, redshifted on the far limb). Downstream from the shock surface only the wake baseline, Eq. 3, is present.

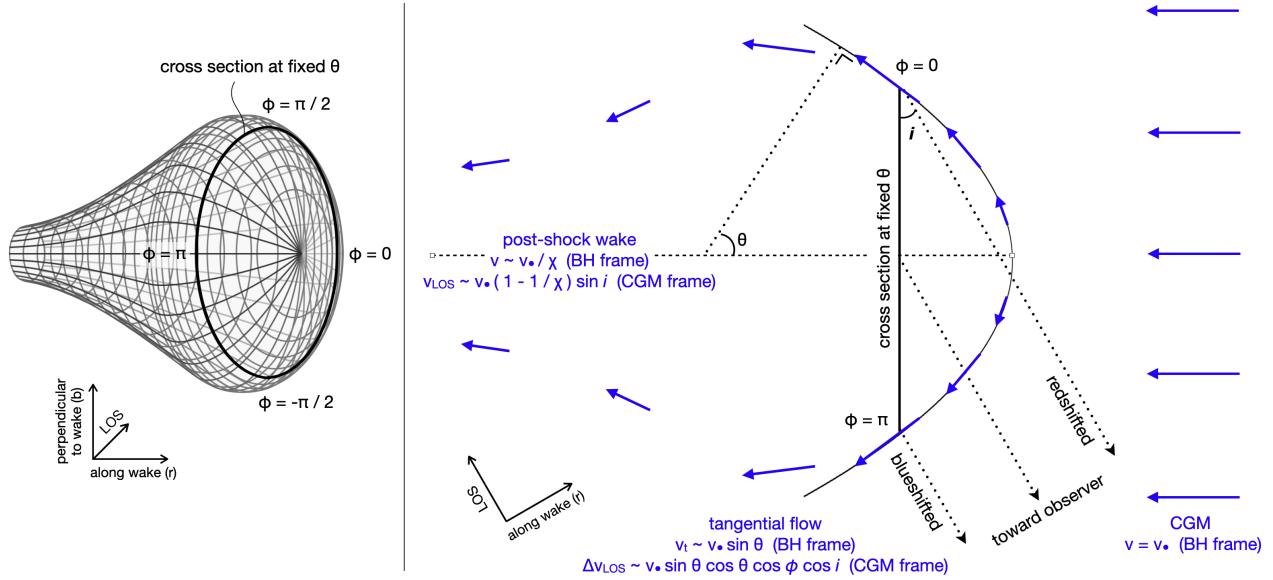


Figure 6. Schematic of our bow shock model, broadly following Wilkin (1996). *Left:* 3D representation of a flow surface, as in Fig. 4. The flow on the shock surface is modeled as a cross-section at a fixed opening angle θ . *Right:* 2D projection. Gas flows, in the rest-frame of the black hole, are indicated with blue arrows. The LOS velocity, in the rest-frame of the CGM, is modeled as the sum of the post-shock wake (which produces the plateau velocity downstream) and the tangential flow. The tangential flow produces a blueshifted component from the near limb and a redshifted component from the far limb.

While simplified, this model (tangential flow on a near-apex paraboloid shell) follows the standard framework for the kinematics of bow shocks (Wilkin 1996; Hartigan et al. 1987).

4.3.2. Turning the 2D Model into a 1D Model

The velocity gradient is measured from spectra collapsed along the projected coordinate b (perpendicular to the wake). We therefore define $x \equiv r - r_0$, with r_0 the center position of the projected cross section along the wake, and average the emission in the model over the chord through the cross section. Inside the region where the flow is on the shock surface ($|x| < a$, with a the projected half-width of the cross section) the LOS-averaged azimuthal factor is

$$\langle \cos \phi \rangle(\xi) = \frac{\xi}{\sqrt{1-\xi^2}} \operatorname{asinh}\left(\frac{\sqrt{1-\xi^2}}{|\xi|}\right), \quad (6)$$

with $\xi \equiv x/a$. This expression encodes the sign flip of the velocities as the near and far sides of the cross section are projected along the line of sight: for $-a < x < 0$ the azimuthal factor is negative and for $0 < x < a$ the factor is positive.

In the 2D \rightarrow 1D projection we also need to account for the spatial distribution of emission within the cross section. Bow shocks are often limb-brightened: the rims contribute more emission than the interior (e.g., Hartigan et al. 1987). To implement rim-brightening we assume a simple local emissivity law within a circular cross section of projected radius a :

$$\epsilon(d_{\text{cross}}) \propto \left(\frac{d_{\text{cross}}}{a}\right)^p, \quad 0 \leq d_{\text{cross}} \leq a, \quad (7)$$

where d_{cross} is the distance from the cross-section center. Thus $p = 0$ gives a uniform “disk” (no limb brightening) and $p > 0$ yields an increasingly rim-dominated “ring”. We adopt $p = 1$ in the baseline and verify that the results are insensitive within reasonable bounds. In the azimuthally-averaged model limb-brightening enters as a weight $W_p(\xi)$, the LOS average of $(d_{\text{cross}}/a)^p$ along the same sightline (so $W_p = 1$ for $p = 0$ and W_p increasing toward the rim for $p > 0$).

The final projected model is then

$$v_{\text{model}}(x) = -v_{\text{LOS, wake}} + v_\bullet \sin \theta \cos \theta \cos i \langle \cos \phi \rangle(x) W_p(x), \quad (8)$$

for $|x| < a$; for $x \leq -a$ (downstream plateau) we set $v_{\text{model}} = -v_{\text{LOS, wake}}$, and we do not compute the model at $x \geq a$ (i.e., upstream from the projected cross section).

4.4. Fitting and Uncertainties

The fit parameters of the model are

$$\{v_\bullet, i, a, r_0\},$$

the black hole velocity, the inclination, the projected half-width of the cross section, and the projected position of the cross section along the wake. The radius of the cross section is calculated from i and a ,

$$R_{\text{ring}} = \frac{a}{\sin i}.$$

The following parameters can be varied but are held fixed in the fit:

$$\{\chi, \theta, p\},$$

the compression factor, the obliquity of the parabola, and the disk/ring geometry of the cross section. The sensitivity of the predicted velocities to the model parameters is discussed in Appendix B, where we also provide a simple relation between the directly-observed velocity amplitudes and the black hole’s velocity and inclination.

We fit Eq. 8 to the observed velocity profile, where we combine the [O III] and H α measurements at $r > 61$ kpc and include the Keck/LRIS data of Paper I at $50 < r < 61$ kpc to anchor the downstream component. We use $\chi = 3$ and $p = 1$. For the obliquity we use $\theta = 60^\circ$; we show in §4.5 that this value is broadly consistent with the morphology of the gas near the apex.⁹ We minimize weighted residuals $(v_{\text{model}} - v)/\sigma_v$ with nonlinear least squares. Inside the canopy we use Eq. 8; on the plateau ($x \leq -a$) we use Eq. 3; $x \geq a$ is masked. Bounds enforce $v_\bullet \geq 0$, $0^\circ < i < 90^\circ$, and $a_{\text{proj}} \geq 0$.

The best-fit profile is compared to the observations in Fig. 7. The fit is good, with reduced $\chi^2 \sim 1$, and has the following values for the key parameters:

$$v_\bullet = 954^{+110}_{-126} \text{ km s}^{-1}, i = 29^{+6}_{-3} \text{ deg}, R_{\text{ring}} = 1.5^{+0.7}_{-0.4} \text{ kpc}.$$

The uncertainties are determined from simulations. The observations are perturbed by their uncertainties in both r and v , and the quoted confidence intervals are the 16th/84th percentiles of the accepted samples. Note that the assumed CGM rest velocity is 0 km s^{-1} , i.e., identical to the velocity of the former host galaxy.

We conclude that the observed kinematics near the apex are consistent with a bow shock produced by an object that is moving at $\sim 1000 \text{ km s}^{-1}$ in a direction that is $\sim 30^\circ$ out of the plane of the sky toward us.

4.5. Comparison to the Photometric Analysis

Here we compare the kinematically-derived spatial extent of the bow shock to that determined in §3 from the parabola fit to the morphology of the [O III] + H α emission. The kinematics are weighted towards the location of the strongest line emission, approximately 2.0 kpc downstream from the apex. Using the best-fitting parabola of §3 with $r_{\text{apex}} \approx 64.6 \text{ kpc}$ and $R_c \approx 1.8 \text{ kpc}$ we find a width of the shock of $R_{\text{phot}} \sim 2.7 \text{ kpc}$.¹⁰ This is somewhat larger than the cross-section radius that was determined from our bow shock model fit to the kinematics, $R_{\text{kin}} = R_{\text{ring}} = 1.5^{+0.7}_{-0.4} \text{ kpc}$. The difference is likely caused by weighting: the emission lines mostly arise in the dense compression zone interior to the shock surface. The photometric obliquity θ_{phot} is related

⁹ As $\Delta v_{\text{LOS}} \propto \sin \theta \cos \theta = \frac{1}{2} \sin 2\theta$, Δv_{LOS} is maximal for $\theta = 45^\circ$.

¹⁰ Note that projection effects are minimal here, in contrast to the dynamical measurement. In the image plane there is foreshortening in the direction along the wake r , but not – to first order – in the perpendicular direction b .

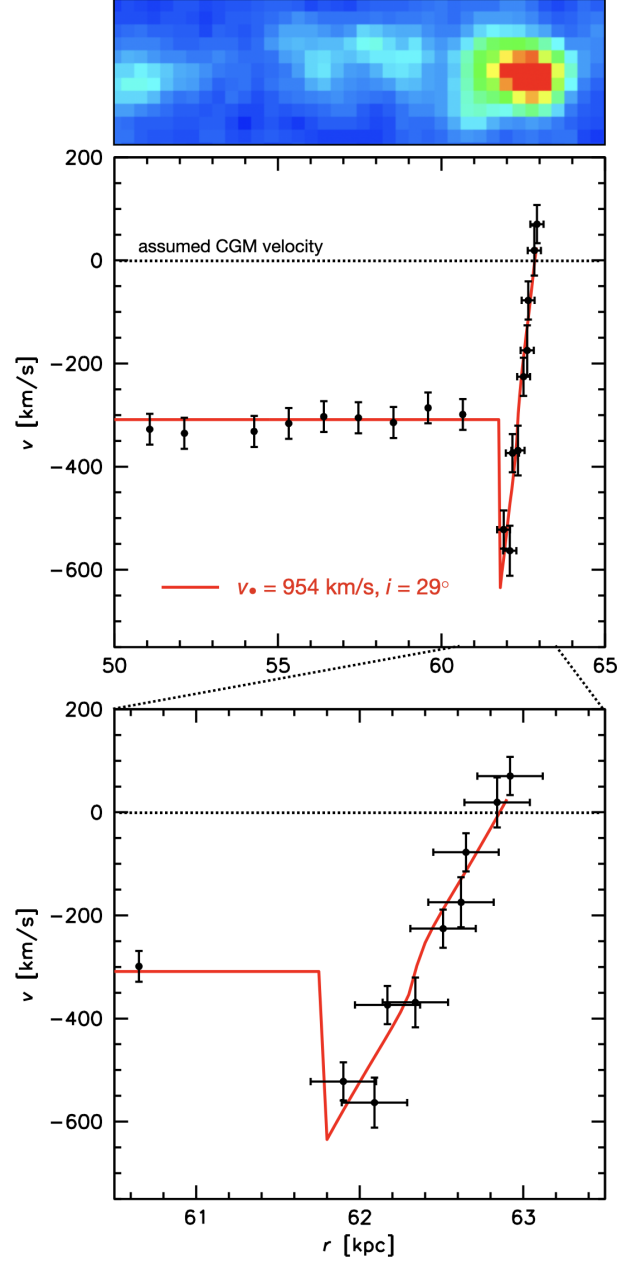


Figure 7. Fit of our bow shock model to the observed kinematics near the apex (solid red line). The data are a combination of the [O III] and H α measurements of Fig. 5 ($r > 61$ kpc) and downstream measurements from the Keck/LRIS spectroscopy of Paper I ($r < 61$ kpc). For reference the [O III] distribution is shown at the top. The model provides an excellent fit to the data, with a reduced $\chi^2 \sim 1$, as it simultaneously explains the plateau velocity of $\approx -300 \text{ km s}^{-1}$ and the steep gradient at the tip.

to R_c through $\theta_{\text{phot}} = \arctan \sqrt{2\Delta r/R_c} \approx 56^\circ$, similar to the assumed $\theta_{\text{kin}} = 60^\circ$.

We conclude that the spatial distribution of ionized gas at the tip of RBH-1 and the dynamical analysis are in reason-

able agreement, particularly when the limitations of our simplistic model are considered.

5. LINE RATIOS

The JWST spectra cover several key diagnostic lines, ranging from [O III] $\lambda 5007$ to [S III] $\lambda 9532$. The strengths of these lines with respect to $H\alpha$ provide independent constraints on the presence of a shock and the velocity of the black hole.

5.1. Observed Line Ratios Near the Tip of the Wake

Line fluxes are measured as a function of position along the wake (r), after summing the flux in the perpendicular direction (b). At $r > 60$ kpc, where the emission lines are relatively bright, the wake is sampled in individual $\Delta r = 0''.05$ pixels. At $r < 60$ kpc we use 2-pixel ($\Delta r = 0''.1$) bins to increase the S/N ratio. Line fluxes are measured by summing the flux in wavelength bins centered on the redshifted line, after subtracting the continuum. The continuum is measured in an adjacent wavelength region; it is generally faint compared to the line flux.

Line ratios are determined by dividing the calibrated line fluxes. We consider [O III]/ $H\alpha$, [N II]/ $H\alpha$, [S II]/ $H\alpha$, and [S III]/[S II]. Here [O III] is [O III] $\lambda 5007$, [N II] is [N II] $\lambda 6584$, [S II] is the sum of the [S II] $\lambda\lambda 6716, 6731$ doublet, and [S III] is the sum of the [S III] $\lambda\lambda 9069, 9532$ doublet.

The observed 1D line ratio profiles at $r > 51$ kpc are shown in Fig. 8, along with corresponding 2D maps. There are clear trends, with [O III]/ $H\alpha$ rising from ≈ 0.6 at ≈ 53 kpc to ≈ 1.5 at the apex; [N II]/ $H\alpha$ low and decreasing slightly, reaching values of ≈ 0.02 near the apex; and [S II] and [S III] moving in opposite directions, with [S II]/ $H\alpha$ sharply decreasing and [S III]/[S II] increasing with r .

5.2. Line Ratio Modeling and Fitting

To interpret the observed emission line ratios along the wake we compare the measurements to a grid of fast radiative shock models generated with the MAPPINGS V code (Sutherland & Dopita 2017, 2018). We use the “shock+precursor” models, allowing the relative weight of the photoionizing precursor to be set with the parameter f_p (where $f_p = 1$ defaults to weighting by the $H\alpha$ luminosity). In our main analysis we use $f_p = 1$.

Several other parameters are also held fixed in the fits, although we explore the sensitivity to them. The preshock density is set to $n_{\text{pre}} = 1$, as the relevant lines are formed when the density reaches $n \gg 1$. As expected, we find that lowering the preshock density to more realistic CGM values ($n = 0.01 - 0.1$) does not change the results but leads to much longer computation times. For the metallicity we adopt SMC-like abundances ($Z \approx 0.2Z_\odot$), broadly consistent with

results from COS-Halos ($Z_{\text{CGM}} \sim 0.1 - 0.5Z_\odot$; Tumlinson et al. 2017; Prochaska et al. 2017). Increasing the metallicity leads to worse fits, particularly for [N II]/ $H\alpha$. In the main analysis we use $f_p = 1$, that is, the relative weight of the components is set by their contribution to the $H\alpha$ luminosity.

We hold the magnetic parameter B fixed to $B = 1$ for our main analysis,¹¹ but ran full grids of temperature and velocity with $B = 0.3$ and $B = 10$. In our fits the magnetic parameter is degenerate with the preshock temperature (such that lower B leads to solutions with higher T_{pre}) and the precursor weight f_p . The parameters B and f_p are knobs that control the preshock ionization; changing them from their defaults produces nearly identical fits but with a different form of $T_{\text{pre}}(r)$.

The two parameters that we *do* allow to vary are the shock velocity v_s and the preshock temperature (with the caveat that T_{pre} is sensitive to the choices for B and f). The model grid spans preshock temperatures $T_{\text{pre}} = 1 \times 10^2 - 3 \times 10^6$ K and shock velocities $v_s = 50 - 2000$ km s⁻¹. Predicted fluxes for all relevant lines ([O III] $\lambda 5007$, [N II] $\lambda 6584$, [S II] $\lambda\lambda 6716, 6731$, and [S III] $\lambda\lambda 9069, 9532$) are normalized to $H\alpha$.

We construct two-dimensional interpolation surfaces $f_i(\log T_{\text{pre}}, \log v_s)$ for each diagnostic ratio i using bicubic interpolation across the model grid. For a given position along the wake (r), we parameterize the preshock temperature and shock velocity as

$$\log T_{\text{pre}}(r) = \begin{cases} \log T_0, & r < r_t, \\ \log T_0 + \alpha(r - r_t), & r \geq r_t, \end{cases} \quad (9)$$

$$\log v_s(r) = \begin{cases} \log v_0, & r < r_t, \\ \log v_0 + \beta(r - r_t), & r \geq r_t, \end{cases} \quad (10)$$

where r_t is a transition radius and $\{T_0, v_0, \alpha, \beta\}$ are free parameters. The best fit is determined by minimizing

$$\chi^2 = \sum_j \sum_i \left[\frac{R_{i,j}^{\text{obs}} - f_i(\log T_{\text{pre}}(r_j), \log v_s(r_j))}{\sigma_{i,j}} \right]^2, \quad (11)$$

where $R_{i,j}^{\text{obs}}$ and $\sigma_{i,j}$ are the observed ratios and their 1σ uncertainties at position r_j .

We find $\log T_0 = 5.6 \pm 0.3$, $\log v_0 = 2.42 \pm 0.05$, $r_t = 54 \pm 2$ kpc, $\alpha = 0.06 \pm 0.05$, and $\beta = 0.026 \pm 0.005$. The best fitting profiles for $T_{\text{pre}}(r)$ and $v_s(r)$, as well as the accompanying spatial variations of the four fitted diagnostics, are shown by the red lines in Fig. 8. The fits reproduce the trends seen in the data reasonably well, although there are significant devi-

¹¹ In MAPPINGS, the magnetic parameter is $B/\sqrt{n_{\text{pre}}}$ with B in μG and n_{pre} in cm^{-3} ; with our choice $n_{\text{pre}} = 1 \text{ cm}^{-3}$, $B = 1$ corresponds to a preshock field $B_0 = 1 \mu\text{G}$.

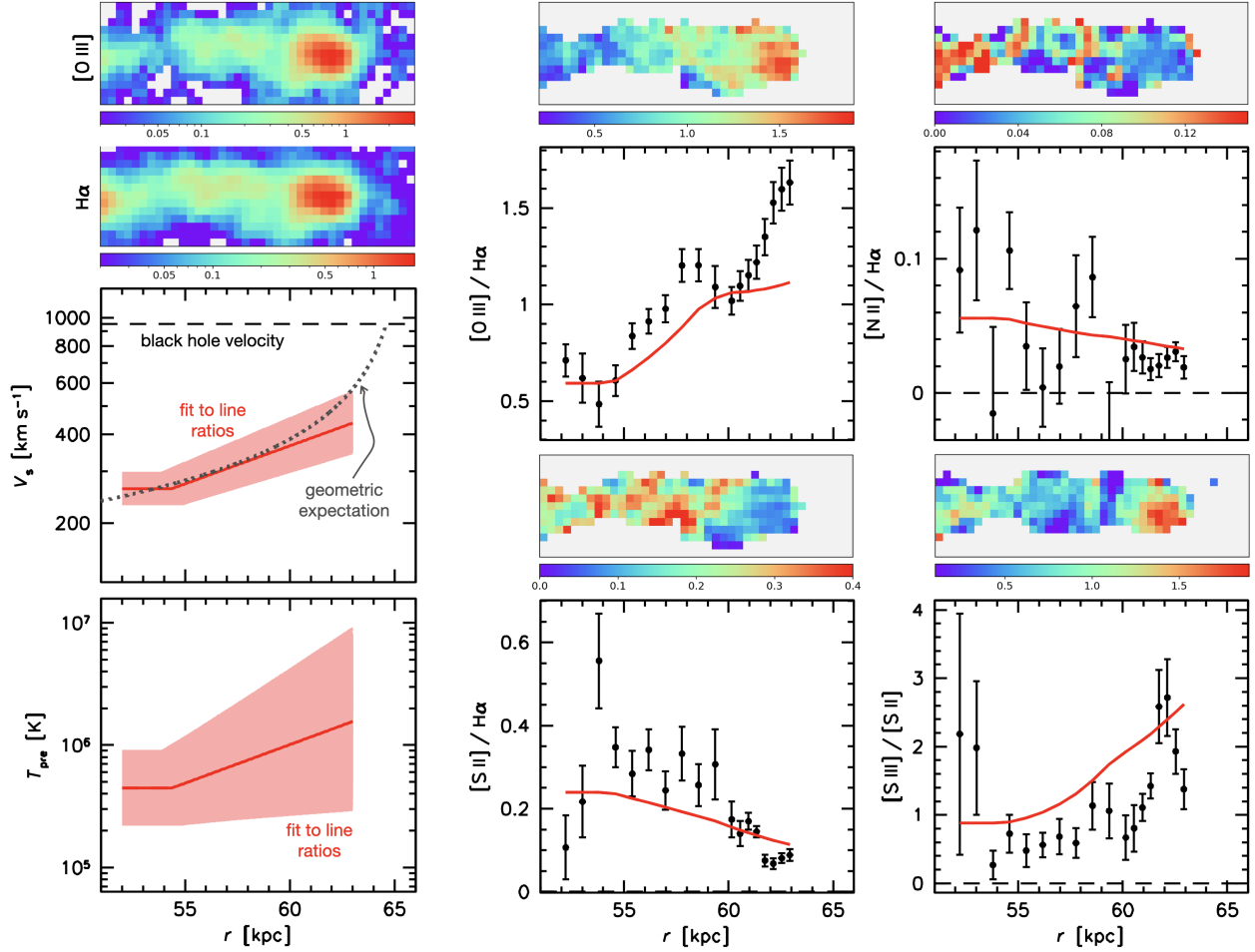


Figure 8. *Left panels:* Mappings model variation in the shock velocity V_s and preshock temperature T_{pre} that produces the fits shown at right. The dotted grey curve shows the expected velocity variation based on the kinematically-derived black hole velocity and the photometricaly-derived shape of the bow shock; it is in good agreement with the Mappings results. *Middle and right panels:* Line ratio maps and line ratio profiles along the wake. There is strong variation, with $[\text{O III}]/\text{H}\alpha$ and $[\text{S III}]/[\text{S II}]$ increasing and $[\text{N II}]$ and $[\text{S II}]$ decreasing toward the tip. Red lines show the best fit Mappings models. They capture the trends, although there are significant local deviations.

ations. These most likely stem from complexity in the morphology and ionization structure of the wake, as is also evident from the spatial variations in the 2D maps. In particular, near the tip of the wake there is a localized “hot spot” where both $[\text{O III}]/\text{H}\alpha$ and $[\text{S III}]/[\text{S II}]$ are elevated (see § 6.4 for further discussion of this region).

The preshock temperature $T_{\text{pre}} \sim 10^6$ K, with considerable uncertainty. This temperature is somewhat higher than expected as optical line formation begins to be efficient at $T \lesssim 10^5$ K. As discussed above we find that increasing f_p or B brings T_{pre} down to this regime; rather than providing meaningful specific values of T_{pre} , the models indicate that strong preshock ionization is required, and this can be achieved in several ways.

5.3. Interpretation of the Shock Velocities

The shock velocities are in the $v_s = 250\text{--}450$ km s $^{-1}$ range, superficially in conflict with the kinematically-derived black

hole velocity of $v_\bullet \sim 950$ km s $^{-1}$. However, they are in fact quite consistent. For a bow shock, the jump conditions depend on the normal component of the flow,

$$v_s(\theta) = v_\bullet \cos \theta, \quad (12)$$

with θ the angle between the symmetry axes and the local surface normal. This is the same angle as the obliquity of the parabola discussed in § 3 and § 4.3.1, and we can therefore relate the expected shock velocity to the morphology of the bow:

$$v_s(r) = v_\bullet \left(1 + \frac{2(r_{\text{apex}} - r)}{R_c} \right)^{-0.5}. \quad (13)$$

The curve for $v_\bullet = 954$ km s $^{-1}$, $r_{\text{apex}} = 64.6$ kpc, and $R_c = 1.8$ kpc is shown by the dotted line in Fig. 8.

The geometric expectation is in excellent agreement with the shock velocities derived from the line ratios, particularly when considering that the two measurements are completely

independent: the red curve is determined from emission line ratios, and the grey dotted curve reflects a combination of a fit to the kinematics (providing v_\bullet) and a fit to the emission line map of the shock (providing r_{apex} and R_c).

6. DISCUSSION

6.1. Origin of the Kiloparsec Scale Bow Shock

The evidence for a supersonic bow shock at the head of RBH-1 is very strong, bordering on overwhelming. The spatial distribution of the line emission, the velocity gradient, and the MAPPINGS analysis of the line ratios are all consistent with a bow shock associated with a compact object moving at $\sim 1000 \text{ km s}^{-1}$ through the CGM. The most direct evidence is the kinematic signature: there is no other plausible explanation for a $\sim 600 \text{ km s}^{-1}$ gradient over $0''.1$. Furthermore, the fact that the wake behind the shock points toward the heart of a galaxy, combined with the 1000 km s^{-1} velocity of the shock, leave little doubt that the compact object in question is a runaway SMBH.

Here we discuss how the bow shock is produced. The most straightforward explanation is the interaction between gas that is gravitationally bound to the black hole and the ambient CGM. However, the observed size of the bow far exceeds this interaction scale. The relevant scale for direct SMBH–gas interaction is the accretion radius,

$$R_{\text{acc}} = \frac{2GM_\bullet}{v_{\text{BH}}^2 + c_s^2} \quad (14)$$

(Bondi & Hoyle 1944; Edgar 2004). For $M_\bullet \sim 2 \times 10^7 M_\odot$, $v_\bullet \sim 10^3 \text{ km s}^{-1}$, and hot CGM with $c_s \sim 200 \text{ km s}^{-1}$, Eq. 14 gives $R_{\text{acc}} \sim 0.2 \text{ pc}$ – four orders of magnitude smaller than the observed kpc-scale bow. The black hole’s gravity is therefore not setting the size or luminosity of the bow shock.

Instead, the shock is likely sustained by momentum balance. In momentum-supported bows the stand-off distance is the location where the outward momentum flux in the gas around the body balances the incoming ram pressure:

$$R_0^2 = \frac{\dot{M}_{\text{out}} v_{\text{out}}}{4\pi \rho_{\text{ext}} v_\bullet^2} \quad (15)$$

(Wilkin 1996; see also van Buren & McCray 1988; Cantó et al. 1996). The spectacular bow shock of Mira (Martin et al. 2007) is a textbook case: a modest AGB wind speed of $5\text{--}10 \text{ km s}^{-1}$ but substantial mass loss makes the product $\dot{M}_{\text{out}} v_{\text{out}}$ large, pushing the bow far from the star.¹² Simulations have successfully reproduced both the observed stand-off scale and the wake morphology of Mira in this framework (Martin et al. 2007; Wareing et al. 2007; Esquivel et al. 2010).

¹² The ratio of Mira’s stand-off distance ($\approx 0.1 \text{ pc}$) to its radius ($\approx 300 R_\odot$) is a factor of $\sim 10^4$.

In our case, the outward pressure is probably not supplied by a true wind coming from the SMBH, at least not consistently. Inverting Eq. 15 and setting $\rho_{\text{ext}} = \mu m_p n_{\text{ext}}$, the outward mass flow required for a kpc-scale stand-off radius is

$$\dot{M}_{\text{out}} \approx \frac{v_\bullet^2}{v_{\text{out}}} 4\pi R_0^2 \mu m_p n_{\text{ext}} \approx 0.26 M_\odot \text{ yr}^{-1} \left(\frac{10^3 \text{ km s}^{-1}}{v_{\text{out}}} \right) \quad (16)$$

for $\mu = 0.62$, $n_{\text{ext}} = 10^{-3} \text{ cm}^{-3}$, $v_\bullet = 954 \text{ km s}^{-1}$, and $R_0 = 1.2 \text{ kpc}$ (see § 3). Even a strong SMBH-driven wind with $v_{\text{out}} \sim 3000 \text{ km s}^{-1}$ requires a mass outflow rate of $\sim 0.1 M_\odot \text{ yr}^{-1}$, corresponding to $\sim 10^7 M_\odot$ since the SMBH left its former host galaxy. Escaping black holes can carry mini-disks with them, but their maximum mass is only a few $\times 10^6 M_\odot$ for $v_\bullet \sim 10^3 \text{ km s}^{-1}$ and $M_\bullet \sim 2 \times 10^7 M_\odot$ (Loeb 2007). Therefore, if the main source of outward pressure were a SMBH-driven wind, it would have been exhausted long ago.

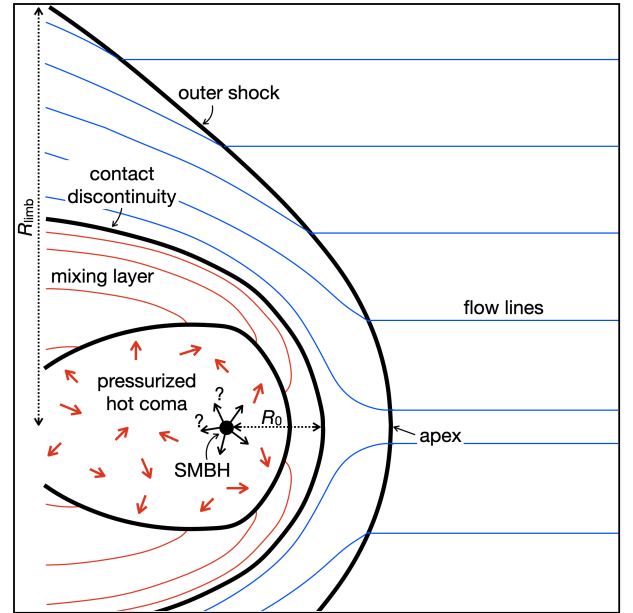


Figure 9. Illustration of the momentum-balanced bow shock that we propose for RBH-1. The figure is adapted from Tarango-Yong & Henney (2018), replacing their stellar wind by a pressure-supported coma. The CGM produces an inward velocity that is captured over the limb cross section R_{limb} . This wind is balanced at the contact discontinuity by pressure from a hot, mass-loaded coma with radius R_0 . Activity associated with the SMBH may provide additional outward pressure.

Momentum balance does not require a true wind, as it can also be achieved by an effective wind generated by a pressurized, mass-loaded coma. This “windless” geometry is illustrated in Fig. 9 and is analogous to cluster cold fronts with bow shocks such as Abell 3667 (Vikhlinin et al. 2001a) and the bullet cluster (Markevitch et al. 2002). In this pic-

ture the relevant outward velocity is the post-shock sound speed of the hot gas at the apex. For a strong adiabatic shock $c_s \approx 0.56v_s$, with v_s the local shock velocity (Sutherland & Dopita 2017).¹³ The shock velocities near the apex are $v_s = 500\text{--}700\text{ km s}^{-1}$ (see Eq. 13), giving an effective outflowing wind of $v_{\text{out}} \approx c_s \approx 300\text{--}400\text{ km s}^{-1}$ and (using Eq. 16) a mass flow of $\approx 0.7 M_\odot \text{ yr}^{-1}$.

The source for this mass is the intercepted CGM, and we can quantify this as

$$\dot{M}_{\text{in}} \approx \rho_{\text{ext}} v_\bullet \pi R_{\text{limb}}^2, \quad (17)$$

where R_{limb} is the effective cross section of the limbs. As Eqs. 15 and 17 both scale with the density, the condition $\dot{M}_{\text{in}} \gtrsim \dot{M}_{\text{out}}$ is satisfied if

$$\frac{R_{\text{limb}}}{R_0} \gtrsim \sqrt{\frac{4v_\bullet}{v_{\text{out}}}}. \quad (18)$$

For our fiducial values of $v_\bullet = 954\text{ km s}^{-1}$, $v_{\text{out}} = 350\text{ km s}^{-1}$, and $R_0 = 1.2\text{ kpc}$, this implies an effective limb radius of $R_{\text{limb}} \gtrsim 4\text{ kpc}$, similar to the cross section of the bow at the location of peak emission ($R_{\text{phot}} \sim 2.7\text{ kpc}$; see § 4.5).

In summary, the bow is maintained by the thermal pressure of the shocked and recycled CGM at the apex, and likely persists in a quasi-steady state for tens of Myr. Continuous inflow and shock heating of the external gas replenishes the hot, mass-loaded coma, which provides the pressure needed to balance the upstream ram pressure. The resulting kiloparsec scale of the shock – far exceeding the SMBH sphere of influence – is set by the momentum budget (see, e.g., Wilkin 1996; Markevitch & Vikhlinin 2007). No wind source beyond the CGM is required to sustain the bow, although it is possible that activity associated with the SMBH contributes to v_{out} . The geometry of the shock surface is governed by Eq. 18; if, for example, black hole activity temporarily boosts v_{out} , the apex becomes overpressured and the stand-off distance R_0 increases in response.

6.2. Origin of the Wake

The feature that initially drew our attention to RBH-1 is not the bow shock but the spectacular wake behind it. Here we discuss the origin of the wake and reinterpret the downstream [O III] velocity trend that we reported in Paper I.

6.2.1. Entrainment and Mixing with the CGM

The wake is highly complex. The emission line gas just behind the bow shock is fragmented into several distinct clumps

¹³ This relation is not given explicitly in Sutherland & Dopita (2017) but it follows from their expression for the post-shock temperature, $T_{\text{ps}} = \frac{3\mu m_p}{16k} v_s^2$, combined with $c_s = \sqrt{\frac{\gamma kT}{\mu m_p}}$, with $\gamma = 5/3$ for an ideal monatomic gas.

(see Fig. 3). Ground-based spectroscopy shows that line emission is present along the entire extent of the wake, with some regions showing clear evidence for ongoing star formation and others exhibiting [O III]/H β ratios indicative of shocks (see Paper I). The radial velocity of the gas shows a strong gradient, going from $\sim -300\text{ km s}^{-1}$ near the tip to $\sim -100\text{ km s}^{-1}$ at $r \sim 20\text{ kpc}$, where $v = 0\text{ km s}^{-1}$ is the radial velocity of the galaxy (see Paper I and Fig. 10). Despite all these turbulent processes the wake remains strikingly narrow over most of its 62 kpc extent, with a radius of $R_{\text{wake}} \approx 0.7\text{ kpc}$.¹⁴ It is also dynamically cold, at least near the tip where we can measure it, with a velocity dispersion of $31 \pm 4\text{ km s}^{-1}$ (see Appendix C).

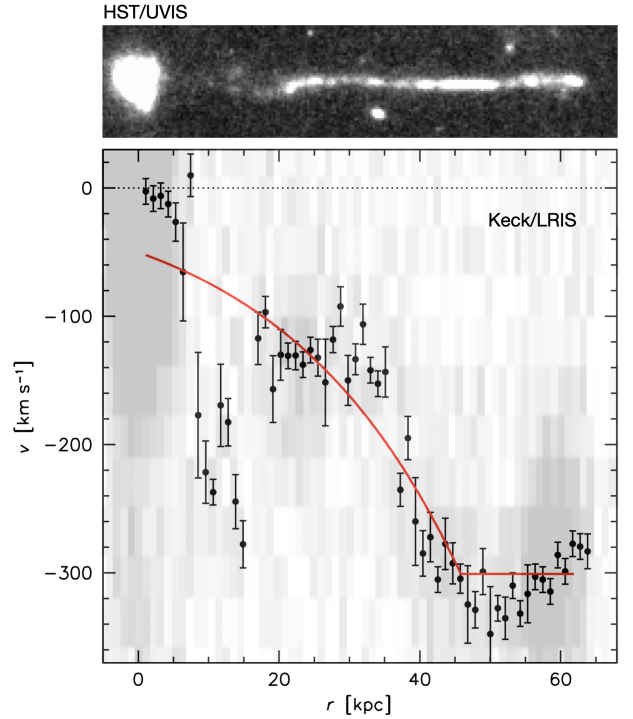


Figure 10. Velocity measurements along the wake, from ground-based [O III] spectroscopy described in Paper I. The 2D LRIS spectrum is shown in light grey. The HST UVIS continuum image is shown at the top for reference. The curve is a delayed-mixing model, with a delay length of $\sim 16\text{ kpc}$ and a mixing length of $\sim 26\text{ kpc}$. These values are broadly consistent with mixing models of cold gas flows in the CGM (see text).

All these features – the coherence of the wake over many kpc, the presence of cold gas far downstream, the evidence for shocks and star formation, and the velocity gradient – are hallmarks of radiative mixing with the CGM. When a thin cold gas stream flows in a hot medium a turbulent mixing layer is established between the cold and the hot gas, with

¹⁴ We set the wake radius as $0.5 \times$ its FWHM in the HST/UVIS image.

the ambient gas becoming entrained and condensing out of the mixing layer. This allows for a long-lived, $T \sim 10^4$ K phase to persist along the wake, with the cold gas mass growing with time (see Gronke & Oh 2018; Ji et al. 2019; Gronke et al. 2022). As the newly added gas has $\langle v \rangle \approx 0 \text{ km s}^{-1}$, the mean absolute velocity of the gas in the wake decreases with time. Where the condensed gas becomes sufficiently dense it can form stars in situ, as has been seen in simulations of stripped tails (Tonnesen & Bryan 2012). These processes are not smooth: in the entrainment framework the turbulence in the mixing layer is often supersonic with respect to the 10^4 K phase, explaining the localized internal shocks and high-excitation patches that are seen within the wake (Scanapieco & Brüggén 2015; Mandelker et al. 2016).

The observed velocity gradient can be compared to predictions for turbulent radiative mixing layers (see, in particular, Tan et al. 2023, for the analogous case of infalling cold gas onto galaxies). Efficient mixing is expected to start after a delay Δt_{delay} , as it takes time for the Kelvin-Helmholtz instabilities to grow and cooling of the mixing layer to become efficient. After that, the cold gas mass is expected to grow exponentially, as the added mass depends on the amount of mass that is already present. Momentum conservation implies that $\dot{v}/v = -\dot{m}/m$, and therefore we have $v(t) = v_0 \exp(-t/t_{\text{grow}})$ with v_0 the initial velocity and t_{grow} defined as $t_{\text{grow}} \equiv m/\dot{m}$.

Motivated by these considerations, and making use of the fact that time corresponds to position along the wake, we fit the following empirical model to the observed velocity gradient:

$$v(r) = v_0 \exp\left(-\frac{\max\{0, (r_\bullet - r) - \Delta r_{\text{delay}}\}}{l_{\text{mix}}}\right), \quad (19)$$

with r the distance from the galaxy along the wake, $r_\bullet \approx 62$ kpc the current position of the black hole, v_0 the plateau velocity immediately behind the black hole, Δr_{delay} the distance behind the black hole where mixing becomes important, and l_{mix} the mixing length. All length scales are in the observed frame, and hence projected. The best fit is shown in Fig. 10. The model provides a reasonable description of the data, although there are significant deviations (particularly in the region $r = 10$ – 20 kpc, where the wake also loses morphological coherence). We find $v_0 = -301 \pm 6 \text{ km s}^{-1}$, $\Delta r_{\text{delay}} = 16 \pm 2$ kpc, and $l_{\text{mix}} = 26 \pm 4$ kpc.

Interpreting these values in terms of time rather than projected distance, we have $\Delta t_{\text{delay}} = \Delta r_{\text{delay}}/(v_\bullet \cos i) \sim 19$ Myr, and $t_{\text{grow}} = l_{\text{mix}}/(v_\bullet \cos i) \sim 31$ Myr. These timescales are consistent with the results of Tan et al. (2023) for radiative mixing of cold gas clouds in a hot ambient medium. Specifically, they find $t_{\text{grow}} \sim 35$ Myr for typical CGM conditions (their Eq. 26). The age of the wake is $t_{\text{wake}} = r_\bullet/(v_\bullet \cos i) \sim 73$ Myr, and we conclude that, for the oldest parts of the wake closest to the galaxy, entrainment has

increased the cold gas mass by a factor of

$$\frac{M}{M_0} \sim \exp\left(\frac{t_{\text{wake}} - \Delta t_{\text{delay}}}{t_{\text{grow}}}\right) \sim 6. \quad (20)$$

6.2.2. Mass Budget: Can Entrainment Explain the Stellar Mass of the Wake?

We now ask whether entrainment provides sufficient cold gas to explain the observed luminosity of the wake. The wake has an F814W AB magnitude of ≈ 22.9 (Paper I). Transforming this into a rest-frame B band luminosity gives $L_B \approx 2 \times 10^{10} L_{\odot, B}$, and assuming that most of the light comes from stars with ages 1–20 Myr and $(M/L)_B \sim 0.01$, we find a total present-day stellar mass of $M_* \sim 2 \times 10^8 M_\odot$. Taking stellar mass loss into account, the total formed mass was $M_{*,0} \approx M_*/0.7 \sim 3 \times 10^8 M_\odot$.

The CGM mass that is intercepted by the bow is $\dot{M}_{\text{in}} \approx 0.7 M_\odot \text{ yr}^{-1}$ for $R_{\text{limb}} \approx 4$ kpc (see § 6.1). Since the SMBH left the galaxy the total intercepted mass is $M_{\text{bow}} \approx t_{\text{wake}} \dot{M}_{\text{in}} \approx 5 \times 10^7 M_\odot$. Taking M_{bow} as the seed for entrainment M_0 , we find a total entrained mass of order $M_{\text{ent}} \sim 6 M_{\text{bow}} \sim 3 \times 10^8 M_\odot$.

While the total cold gas mass and the stellar mass appear to be in good agreement, this is only the case for an unreasonably efficient gas \rightarrow stars conversion. The highest conversion rates occur in starburst galaxies, which have gas depletion times of $t_{\text{dep}} = 0.2 \pm 0.1$ Gyr (Genzel et al. 2010). Even with this depletion time, the maximum star formation efficiency over the ≈ 70 Myr lifetime of the wake would be $\epsilon_{\text{max}} \approx 1 - \exp(-70/200) \approx 0.3$, with $\int_i M_* = \epsilon \int_i M_{\text{gas}}$. The stellar mass that can form out of the entrained gas is therefore $M_* \lesssim 0.3 M_{\text{ent}} \lesssim 1 \times 10^8 M_\odot$. We conclude that the stellar mass that can be produced by the entrained gas is at least a factor of several lower than the observed stellar mass, for our default assumptions.

There are several ways to resolve this mild discrepancy, such as a higher CGM density (as $\dot{M}_{\text{in}} \propto \rho_{\text{ext}}$) or a larger cross section of the bow. An interesting possibility is that the stellar initial mass function (IMF) is modestly top-heavy, thus lowering the M/L ratio of the wake. A relatively high background temperature may raise the turnover mass of the IMF due to the $T^{3/2}$ dependence of the Jeans mass (Larson 1998; Krumholz 2006; Bate 2009, 2023). Top-heavy IMFs have been observed in some other extreme environments, such as the 30 Doradus cluster (Schneider et al. 2018) and the central 300 pc of the Milky Way (Lu et al. 2013; Hosek et al. 2019).

6.3. Black Hole Mass Estimate from Energy Conservation

It is perhaps surprising that the black hole mass does not enter the analysis of § 6.1: the expression for the geometry of the bow shock depends on the velocity of the SMBH and the effective counteracting wind only. The SMBH plays an important role behind the scenes: its gravity keeps a few-

pc core bound and centered, preventing the stagnation point from wandering and thereby stabilizing the coma and bow-shock geometry. The mass likely also mattered during the initial growth phase, as gas that escaped with the black hole may have seeded the bow. Ablation and mixing of this gas with the CGM pressurized the coma until momentum balance with the ram pressure was reached. Once that happened, the bow became self-sustaining.

Although we cannot directly measure the mass of the SMBH from the observed shock, the fact that the shock has persisted for $t_{\text{wake}} \sim 70$ Myr provides an interesting constraint. The bow continuously thermalizes the kinetic energy of the CGM at a rate similar to the ram-pressure power (e.g., [Vikhlinin et al. 2001b](#); [Markevitch & Vikhlinin 2007](#)):

$$\dot{E}_{\text{heat}} \sim \rho_{\text{ext}} v_{\bullet}^3 \pi R_0^2. \quad (21)$$

Over the wake lifetime t_{wake} , the total processed kinetic energy is therefore

$$E_{\text{heat}} \sim \varepsilon \rho_{\text{ext}} v_{\bullet}^3 \pi R_0^2 t_{\text{wake}}, \quad (22)$$

where $\varepsilon \sim 1$ is the fraction of ram power deposited into the hot phase. The ultimate source of this heating is the kinetic energy of the SMBH, and we have $E_{\bullet} = \frac{1}{2} M_{\bullet} v_{\bullet}^2 \gtrsim E_{\text{heat}}$. Rewriting this in terms of a mass limit, we obtain

$$M_{\bullet} \gtrsim 2 \varepsilon \rho_{\text{ext}} v_{\bullet} \pi R_0^2 t_{\text{wake}}. \quad (23)$$

For our fiducial values $n_{\text{ext}} = 10^{-3} \text{ cm}^{-3}$, $v_{\bullet} = 954 \text{ km s}^{-1}$, $R_0 = 1.2 \text{ kpc}$, and $t_{\text{wake}} = 73 \text{ Myr}$, Eq. 23 gives $M_{\bullet} \gtrsim \text{a few} \times 10^7 M_{\odot}$.

Interestingly, this mass is similar to the SMBH mass of $M_{\bullet} \sim 2 \times 10^7 M_{\odot}$ that is implied by the bulge mass of the former host galaxy (see Paper I and [Schutte et al. 2019](#)). This similarity implies that the SMBH may have slowed down somewhat since its escape. Furthermore, it suggests that gravitational wave recoil is a more likely escape mechanism than a three-body interaction. Recoil causes the merged remnant black hole to escape, leaving a black hole-less galaxy behind. In three-body interactions only one of the three SMBHs generally escapes, and it is the lowest mass SMBH of the three that has the highest escape probability (e.g., [Hoffman & Loeb 2007](#)). In this scenario it is unlikely that the mass of the escaped SMBH is similar to the *total* SMBH mass that is implied by the bulge mass– M_{\bullet} scaling relation.

6.4. Can We See the Black Hole?

All observational signatures that we have discussed in this paper so far are caused by the bow shock and not by the SMBH itself.¹⁵ We already knew that the black hole is not

very active: in Paper I we examined publicly available Chandra and VLA data, finding no significant signal near the tip of the wake. When we wrote the JWST proposal we expressed hope that we might detect the SMBH even if it is not active, through gas that is bound to it; in that case we would see a point source with relatively broad ($\text{FWHM} \gtrsim 500 \text{ km s}^{-1}$) emission lines. A careful search of the data cube near the tip does not show such an object. Moreover, it may not be possible to detect bound gas even if it exists: in the geometry of Fig. 9 the SMBH is inside a hot ($T \gtrsim 10^6 \text{ K}$) coma that suppresses optical line formation.

We do find tentative evidence for emission originating from the SMBH, not in the JWST spectra but in the HST/UVIS LP_{diff} UV image. As explained in § 2.1 the LP_{diff} band is obtained by subtracting two long pass filters, $\text{LP}_{\text{diff}} = \text{F200LP} - 1.22 \times \text{F350LP}$, creating a broad UV filter with central rest-frame wavelength $\lambda_{\text{rest}} \sim 1400 \text{ \AA}$. It is the most sensitive UV filter on HST but it is not very “clean”, as the F200LP and F350LP bands are not identical beyond 3500 \AA . as a result, LP_{diff} contains varying amounts of light from long wavelengths depending on the color of the object, and is almost impossible to calibrate.

With these caveats in mind, we show the LP_{diff} image in the top panel of Fig. 11. The wake shows regions of diffuse emission, particularly just behind the tip, and several distinct knots. The interpretation of the downstream knots is straightforward: they coincide with star forming regions that we identified in Paper I based on their (ground-based) emission line ratios.

There is also a knot at the tip of the wake. This may be a star forming region as well, but the line ratios in that vicinity are inconsistent with that interpretation (see § 5). A zoomed-in view is shown in the main panel of Fig. 11. Intriguingly, while the UV knot is offset from the peak of the line emission, it is in the expected location for the SMBH: on the symmetry axis, at a distance $R_0 = 1 - 2 \text{ kpc}$ behind the apex of the shock surface (see Fig. 9). We tentatively identify the UV source as emission from the vicinity of the SMBH itself, although this has to be confirmed with follow-up UV imaging or spectroscopy.

We note that the line ratio analysis provides circumstantial support for this interpretation. As discussed in § 5, there is a small region near the tip where the $[\text{O III}]/\text{H}\alpha$ and $[\text{S III}]/[\text{S II}]$ ratios are elevated. In that patch the observed $[\text{O III}]/\text{H}\alpha$ exceeds the values from shock + precursor models ([Sutherland & Dopita 2017](#)), indicating an additional source of hard ionizing photons. This patch is $0''.1$ from the UV source and it could be that photons from the SMBH illuminate the inside of the mixing layer at that location. Further circumstantial support comes from the fact that even weakly-active SMBHs can launch large-scale winds (see, e.g., [Che-](#)

¹⁵ The black hole is the Wizard behind the curtain: it is the unseen mover setting the boundary conditions, but what we actually observe is the shocked CGM.

ung et al. 2016; Cazzoli et al. 2022), thus making it easier to balance the external ram pressure (see § 6.1).

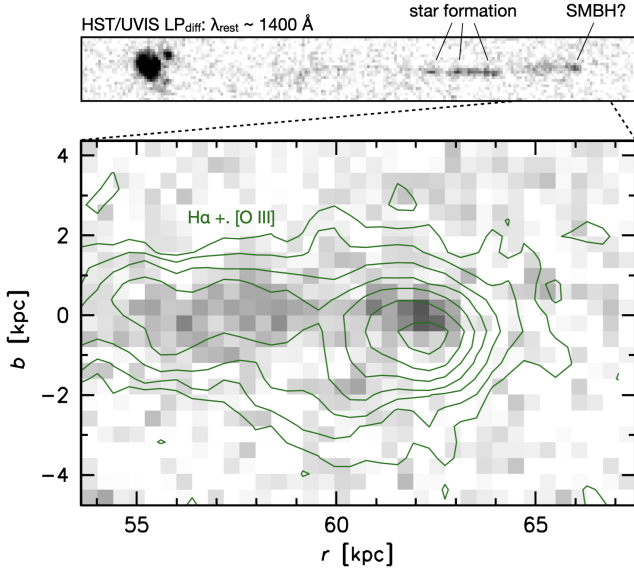


Figure 11. *Top panel:* HST/UVIS far-UV image of RBH-1, in the broad LP_{diff} passband. The wake shows several downstream knots that are associated with star forming regions (see Paper I). There is a compact UV source near the tip of the wake, which may be emission from the vicinity of the SMBH. *Main panel:* Zoom-in on the tip region, with contours showing the [O III] + H α line emission. The UV knot is in the expected location for the SMBH, 1–2 kpc behind the apex. It is slightly offset from the peak of the line emission.

6.5. Revisiting Paper I

With the additional information from the HST/UVIS imaging and the JWST/NIRSpec spectroscopy we briefly discuss what aspects of the analysis in Paper I are confirmed or refuted by the new data.

The central proposal of Paper I was that the linear feature is the wake behind a runaway supermassive black hole, and this is strongly supported by our analysis. We also confirm the presence of a spatially-resolved bow shock at the head of the wake, something that we predicted based on shock models and the luminosity of the [O III] knot in the Keck/LRIS data.

What we did *not* get right is the interpretation of the [O III] velocity curve. We assumed that the CGM remains unperturbed by the wake except for small perpendicular gravitational accelerations, as in the de la Fuente Marcos & de la Fuente Marcos (2008) and Ogiya & Nagai (2024) models, and it did not occur to us to interpret the ionized gas as a post-shock flow with velocity $\approx (1 - 1/r)v_{\bullet}$. Instead, we suggested that ionizing radiation from the shock and the wake illuminates the CGM and that the data probe the local CGM kinematics. We did realize this was problematic, as the velocity trend exceeds the estimated virial velocity of the halo

($V_{\text{vir}} \approx 130 \text{ km s}^{-1}$).¹⁶ Our interpretation of “wiggles” in the morphology as evidence of buffeting by the CGM is also wrong (§ 7.2 in Paper I). There is no need for a complex explanation; in the radiative cooling/entrainment picture local clumping and displacements are expected, due to the turbulent nature of the process.

Importantly, we find no evidence for a proposed “counter” wake, on the other side of the galaxy. We tentatively detected this feature in [O III] and a ground-based CFHT u band image. If the CFHT detection were real, the feature should have been quite bright in our deep HST/UVIS F200LP and F350LP data, but it is undetected. This was also reported by Montes et al. (2024), who performed an archival study of the UVIS data. The proposed counter wake is also undetected in the deep VLT B band imaging discussed in van Dokkum (2023). The lack of a counter feature resolves an awkward coincidence that we highlighted in Paper I: dual escapes of SMBHs are possible but rare compared to single escapes, occurring in only $\sim 1\%$ of three-body interactions (Hoffman & Loeb 2007).

Finally, the stellar population analysis of § 7.1 may or may not be correct. We interpreted the strong color variation along the wake as alternating dominance of blue and red supergiants, with stellar population ages that increase monotonically with distance from the black hole. That interpretation likely holds qualitatively, but the distance \rightarrow age model that we fitted is probably too simplistic. In the entrainment picture, star formation not only occurs just behind the tip but downstream as well, as new gas is continuously added to the wake. We see direct evidence for this in the UV image. A broad age gradient is still expected, as the black hole passage sets a maximum age of $(r_{\bullet} - r)/(v_{\bullet} \cos i)$ at any position along the wake. A re-analysis of the continuum emission, making use of the new HST imaging and JWST spectra, is possible but beyond the scope of the present paper.

7. CONCLUSIONS

Using newly obtained HST/UVIS and JWST/NIRSpec data we confirm that the remarkable linear feature reported in Paper I is the wake behind a runaway SMBH. The single strongest piece of evidence is a $\sim 600 \text{ km s}^{-1}$ velocity gradient over $0''.1$ at the tip of the feature. We dub the object RBH-1, recognizing that it is the first confirmed runaway SMBH. RBH-1 is imperial validation of the 50-year old prediction that SMBHs can escape from their host galaxies, through gravitational wave recoil (Bekenstein 1973) or a three-body interaction (Saslaw et al. 1974).

¹⁶ We also realized that the CGM had to be dynamically cold in our explanation; as shown in Appendix C the velocity dispersion of the gas is only $\approx 30 \text{ km s}^{-1}$. We therefore suggested that the wake was illuminating a cold filament in the CGM.

Wakes may be a generic feature of runaway black holes, as all that may be needed is a small initial gas reservoir to seed the coma and bow. If so, their demographics can directly constrain the frequency and velocity distribution of SMBH ejections. RBH-1 is difficult to identify in ground-based imaging data as its extreme axis ratio of ≈ 50 is reduced by an order of magnitude in typical seeing conditions. The obvious

data sets to look for these features in a systematic way are wide-field surveys with Euclid and Roman.

ACKNOWLEDGEMENTS

We thank Daisuke Nagai and Go Ogiya for useful discussions in the early stages of this project. Support from grants HST-GO-17301 and JWST-GO-3149 is gratefully acknowledged. The data from these programs can be retrieved using DOI [10.17909/8d8q-r813](https://doi.org/10.17909/8d8q-r813).

REFERENCES

- Anderson, J. D. 2003, *Modern Compressible Flow: With Historical Perspective*, 3rd edn. (New York: McGraw-Hill)
- Bally, J., Heathcote, S., Reipurth, B., et al. 2002, *AJ*, 123, 2627, doi: [10.1086/339837](https://doi.org/10.1086/339837)
- Bate, M. R. 2009, *MNRAS*, 392, 1363, doi: [10.1111/j.1365-2966.2008.14165.x](https://doi.org/10.1111/j.1365-2966.2008.14165.x)
- . 2023, *MNRAS*, 519, 688, doi: [10.1093/mnras/stac3481](https://doi.org/10.1093/mnras/stac3481)
- Bekenstein, J. D. 1973, *ApJ*, 183, 657, doi: [10.1086/152255](https://doi.org/10.1086/152255)
- Bondi, H., & Hoyle, F. 1944, *MNRAS*, 104, 273, doi: [10.1093/mnras/104.5.273](https://doi.org/10.1093/mnras/104.5.273)
- Boylan-Kolchin, M., Ma, C.-P., & Quataert, E. 2004, *ApJL*, 613, L37, doi: [10.1086/425073](https://doi.org/10.1086/425073)
- Bucciantini, N. 2002, *A&A*, 387, 1066, doi: [10.1051/0004-6361:20020495](https://doi.org/10.1051/0004-6361:20020495)
- Bushouse, H., Eisenhamer, J., Dencheva, N., et al. 2025, *JWST Calibration Pipeline*, Zenodo, doi: [10.5281/ZENODO.15178003](https://doi.org/10.5281/ZENODO.15178003)
- Campanelli, M., Lousto, C., Zlochower, Y., & Merritt, D. 2007, *The Astrophysical Journal*, 659, L5, doi: [10.1086/516712](https://doi.org/10.1086/516712)
- Cantó, J., Raga, A. C., & Wilkin, F. P. 1996, *ApJ*, 469, 729, doi: [10.1086/177823](https://doi.org/10.1086/177823)
- Cazzoli, S., Hermosa Muñoz, L., Márquez, I., et al. 2022, *A&A*, 664, A135, doi: [10.1051/0004-6361/202142695](https://doi.org/10.1051/0004-6361/202142695)
- Chen, N., LaChance, P., Ni, Y., et al. 2023, *ApJL*, 954, L2, doi: [10.3847/2041-8213/aced45](https://doi.org/10.3847/2041-8213/aced45)
- Cheung, E., Bundy, K., Cappellari, M., et al. 2016, *Nature*, 533, 504, doi: [10.1038/nature18006](https://doi.org/10.1038/nature18006)
- Chiaberge, M., Ely, J. C., Meyer, E. T., et al. 2017, *A&A*, 600, A57, doi: [10.1051/0004-6361/201629522](https://doi.org/10.1051/0004-6361/201629522)
- Civano, F., Elvis, M., Lanzuisi, G., et al. 2010, *ApJ*, 717, 209, doi: [10.1088/0004-637X/717/1/209](https://doi.org/10.1088/0004-637X/717/1/209)
- de la Fuente Marcos, R., & de la Fuente Marcos, C. 2008, *ApJL*, 677, L47, doi: [10.1086/587962](https://doi.org/10.1086/587962)
- Dopita, M. A., & Sutherland, R. S. 1996, *ApJS*, 102, 161, doi: [10.1086/192255](https://doi.org/10.1086/192255)
- Draine, B. T. 2011, *Physics of the Interstellar and Intergalactic Medium* (Princeton University Press)
- Draine, B. T., & McKee, C. F. 1993, *Annual Review of Astronomy and Astrophysics*, 31, 373, doi: [10.1146/annurev.aa.31.090193.002105](https://doi.org/10.1146/annurev.aa.31.090193.002105)
- Edgar, R. G. 2004, *New Astronomy Reviews*, 48, 843, doi: [10.1016/j.newar.2004.06.001](https://doi.org/10.1016/j.newar.2004.06.001)
- Esquivel, A., Raga, A. C., Cantó, J., et al. 2010, *ApJ*, 725, 1466, doi: [10.1088/0004-637X/725/2/1466](https://doi.org/10.1088/0004-637X/725/2/1466)
- Genzel, R., Tacconi, L. J., Gracia-Carpio, J., et al. 2010, *MNRAS*, 407, 2091, doi: [10.1111/j.1365-2966.2010.16969.x](https://doi.org/10.1111/j.1365-2966.2010.16969.x)
- Gronke, M., & Oh, S. P. 2018, *Monthly Notices of the Royal Astronomical Society*, 480, L111
- Gronke, M., Oh, S. P., Ji, S., & Norman, C. 2022, *Monthly Notices of the Royal Astronomical Society*, 512, 2530
- Hartigan, P., Raymond, J., & Hartmann, L. 1987, *ApJ*, 316, 323, doi: [10.1086/165204](https://doi.org/10.1086/165204)
- Hartigan, P., Raymond, J., & Hartmann, S. 1987, *Astrophys. J.*, 316, 323, doi: [10.1086/165204](https://doi.org/10.1086/165204)
- Hoffman, L., & Loeb, A. 2007, *MNRAS*, 377, 957, doi: [10.1111/j.1365-2966.2007.11694.x](https://doi.org/10.1111/j.1365-2966.2007.11694.x)
- Hosek, Matthew W., J., Lu, J. R., Anderson, J., et al. 2019, *ApJ*, 870, 44, doi: [10.3847/1538-4357/aaf90](https://doi.org/10.3847/1538-4357/aaf90)
- Indebetouw, R., & Noriega-Crespo, A. 1995, *AJ*, 109, 752, doi: [10.1086/117318](https://doi.org/10.1086/117318)
- Ji, S., Oh, S. P., & Masterson, P. 2019, *Nature Astronomy*, 3, 808
- Komossa, S., Zhou, H., & Lu, H. 2008, *ApJL*, 678, L81, doi: [10.1086/588656](https://doi.org/10.1086/588656)
- Krumholz, M. R. 2006, *ApJL*, 641, L45, doi: [10.1086/503771](https://doi.org/10.1086/503771)
- Larson, R. B. 1998, *MNRAS*, 301, 569
- Li, M., Emonts, B. H. C., Cai, Z., et al. 2025, *arXiv e-prints*, arXiv:2506.10058, doi: [10.48550/arXiv.2506.10058](https://doi.org/10.48550/arXiv.2506.10058)
- Liu, Y., An, T., Mezcua, M., et al. 2025, *arXiv e-prints*, arXiv:2508.17293, doi: [10.48550/arXiv.2508.17293](https://doi.org/10.48550/arXiv.2508.17293)
- Loeb, A. 2007, *Physical Review Letters*, 99, 041103, doi: [10.1103/PhysRevLett.99.041103](https://doi.org/10.1103/PhysRevLett.99.041103)
- López-Martín, L., López, J. A., Esteban, C., et al. 2002, *A&A*, 388, 652, doi: [10.1051/0004-6361:20020502](https://doi.org/10.1051/0004-6361:20020502)

- Lousto, C. O., Zlochower, Y., Dotti, M., & Volonteri, M. 2012, *PhRvD*, 85, 084015, doi: [10.1103/PhysRevD.85.084015](https://doi.org/10.1103/PhysRevD.85.084015)
- Lu, J. R., Do, T., Ghez, A. M., et al. 2013, *ApJ*, 764, 155, doi: [10.1088/0004-637X/764/2/155](https://doi.org/10.1088/0004-637X/764/2/155)
- Mack, J., Bajaj, V., Khandrika, H., & MacKenty, J. 2016, WFC3/UVIS 2.0: Chip-Dependent Flats, Instrument Science Report WFC3-2016-04, Space Telescope Science Institute. https://www.stsci.edu/files/live/sites/www/files/home/hst/instrumentation/wfc3/documentation/instrument-science-reports-isrs/_documents/2016/WFC3-2016-04.pdf
- Magain, P., Letawe, G., Courbin, F., et al. 2005, *Nature*, 437, 381, doi: [10.1038/nature04013](https://doi.org/10.1038/nature04013)
- Mandelker, N., Padnos, D., Dekel, A., et al. 2016, *Monthly Notices of the Royal Astronomical Society*, 463, 3921
- Markevitch, M., Gonzalez, A. H., David, L., et al. 2002, *ApJ Letters*, 567, L27, doi: [10.1086/339619](https://doi.org/10.1086/339619)
- Markevitch, M., & Vikhlinin, A. 2007, *Physics Reports*, 443, 1, doi: [10.1016/j.physrep.2007.01.001](https://doi.org/10.1016/j.physrep.2007.01.001)
- Martin, D. C., et al. 2007, *Nature*, 448, 780, doi: [10.1038/nature06003](https://doi.org/10.1038/nature06003)
- Martin, N. F., Ibata, R. A., Chapman, S. C., Irwin, M., & Lewis, G. F. 2007, *MNRAS*, 380, 281, doi: [10.1111/j.1365-2966.2007.12055.x](https://doi.org/10.1111/j.1365-2966.2007.12055.x)
- Merritt, D., Schnittman, J. D., & Komossa, S. 2009, *ApJ*, 699, 1690, doi: [10.1088/0004-637X/699/2/1690](https://doi.org/10.1088/0004-637X/699/2/1690)
- Merritt, D., Storch-Bergmann, T., Robinson, A., et al. 2006, *MNRAS*, 367, 1746, doi: [10.1111/j.1365-2966.2006.10093.x](https://doi.org/10.1111/j.1365-2966.2006.10093.x)
- Meyer, D. M.-A., Mignone, A., Kuiper, R., Raga, A. C., & Kley, W. 2017, *MNRAS*, 464, 3229, doi: [10.1093/mnras/stw2537](https://doi.org/10.1093/mnras/stw2537)
- Montes, M., Sánchez Almeida, J., & Trujillo, I. 2024, *Research Notes of the American Astronomical Society*, 8, 150, doi: [10.3847/2515-5172/ad530b](https://doi.org/10.3847/2515-5172/ad530b)
- Ogiya, G., & Nagai, D. 2024, *MNRAS*, 527, 5503, doi: [10.1093/mnras/stad3469](https://doi.org/10.1093/mnras/stad3469)
- Prochaska, J. X., Werk, J. K., Worseck, G., et al. 2017, *Astrophysical Journal*, 837, 169, doi: [10.3847/1538-4357/aa6007](https://doi.org/10.3847/1538-4357/aa6007)
- Rauscher, B. J. 2024, *PASP*, 136, 015001, doi: [10.1088/1538-3873/ad1b36](https://doi.org/10.1088/1538-3873/ad1b36)
- Reipurth, B., Heathcote, S., Morse, J., Hartigan, P., & Bally, J. 2002, *AJ*, 123, 362, doi: [10.1086/324738](https://doi.org/10.1086/324738)
- Ricarte, A., Tremmel, M., Natarajan, P., Zimmer, C., & Quinn, T. 2021, *MNRAS*, 503, 6098, doi: [10.1093/mnras/stab866](https://doi.org/10.1093/mnras/stab866)
- Rigby, J. R., Vieira, J. D., Phadke, K. A., et al. 2023, JWST Early Release Science Program TEMPLATES: Targeting Extremely Magnified Panchromatic Lensed Arcs and their Extended Star formation. <https://arxiv.org/abs/2312.10465>
- Robinson, A., Young, S., Axon, D. J., Kharb, P., & Smith, J. E. 2010, *ApJL*, 717, L122, doi: [10.1088/2041-8205/717/2/L122](https://doi.org/10.1088/2041-8205/717/2/L122)
- Sánchez Almeida, J., Montes, M., & Trujillo, I. 2023, *A&A*, 673, L9, doi: [10.1051/0004-6361/202346430](https://doi.org/10.1051/0004-6361/202346430)
- Saslaw, W. C., & De Young, D. S. 1972, *Astrophys. Lett.*, 11, 87
- Saslaw, W. C., Valtonen, M. J., & Aarseth, S. J. 1974, *ApJ*, 190, 253, doi: [10.1086/152870](https://doi.org/10.1086/152870)
- Scannapieco, E., & Brüggen, M. 2015, *Astrophysical Journal*, 805, 158
- Schneider, F. R. N., Sana, H., Evans, C. J., et al. 2018, *Science*, 359, 69, doi: [10.1126/science.aan0106](https://doi.org/10.1126/science.aan0106)
- Schutte, Z., Reines, A. E., & Greene, J. E. 2019, *ApJ*, 887, 245, doi: [10.3847/1538-4357/ab35dd](https://doi.org/10.3847/1538-4357/ab35dd)
- Sutherland, R. S., & Dopita, M. A. 2017, *ApJS*, 229, 34, doi: [10.3847/1538-4365/aa6541](https://doi.org/10.3847/1538-4365/aa6541)
- Tan, B., Oh, S. P., & Gronke, M. 2023, *MNRAS*, 520, 2571, doi: [10.1093/mnras/stad236](https://doi.org/10.1093/mnras/stad236)
- Tarango-Yong, J. A., & Henney, W. J. 2018, *MNRAS*, 477, 2431, doi: [10.1093/mnras/sty669](https://doi.org/10.1093/mnras/sty669)
- Tonnesen, S., & Bryan, G. L. 2012, *Monthly Notices of the Royal Astronomical Society*, 422, 1609
- Tumlinson, J., Peebles, M. S., & Werk, J. K. 2017, *Annual Review of Astronomy and Astrophysics*, 55, 389, doi: [10.1146/annurev-astro-091916-055240](https://doi.org/10.1146/annurev-astro-091916-055240)
- van Buren, D., & McCray, R. 1988, *ApJ*, 329, L93, doi: [10.1086/185167](https://doi.org/10.1086/185167)
- van Dokkum, P. 2023, *Research Notes of the American Astronomical Society*, 7, 83, doi: [10.3847/2515-5172/acd196](https://doi.org/10.3847/2515-5172/acd196)
- van Dokkum, P., Brammer, G., Baggen, J. F. W., et al. 2025a, *arXiv e-prints*, arXiv:2506.15618, doi: [10.48550/arXiv.2506.15618](https://doi.org/10.48550/arXiv.2506.15618)
- van Dokkum, P., Brammer, G., Jennings, C., Pasha, I., & Baggen, J. F. W. 2025b, *ApJL*, 990, L48, doi: [10.3847/2041-8213/adfb50](https://doi.org/10.3847/2041-8213/adfb50)
- van Dokkum, P., Pasha, I., Buzzo, M. L., et al. 2023, *ApJL*, 946, L50, doi: [10.3847/2041-8213/acba86](https://doi.org/10.3847/2041-8213/acba86)
- Vikhlinin, A., Markevitch, M., & Murray, S. S. 2001a, *ApJ*, 551, 160, doi: [10.1086/320078](https://doi.org/10.1086/320078)
- . 2001b, *ApJ*, 551, 160
- Volonteri, M., Haardt, F., & Madau, P. 2003, *ApJ*, 582, 559, doi: [10.1086/344675](https://doi.org/10.1086/344675)
- Wareing, C. J., Zijlstra, A. A., & O'Brien, T. J. 2007, *MNRAS*, 382, 1233, doi: [10.1111/j.1365-2966.2007.12447.x](https://doi.org/10.1111/j.1365-2966.2007.12447.x)
- Wilkin, F. P. 1996, *Astrophys. J. Lett.*, 459, L31, doi: [10.1086/309939](https://doi.org/10.1086/309939)

APPENDIX

A. THE VELOCITY GRADIENT INTERPRETED AS THE GRAVITATIONAL INFLUENCE OF THE BLACK HOLE

In the main text we interpret the steep velocity gradient near the apex in the context of a bow shock model. Here we ask whether the gradient could be caused by the gravitational influence of the SMBH – either from gas that is bound to the SMBH and escaped with it (see Boylan-Kolchin et al. 2004; Merritt et al. 2009), or from kicks imparted on the gas as the black hole passes (see Ogiya & Nagai 2024).

We find that the spatial extent of the gradient is at least an order of magnitude too large. We express this in terms of the derived black hole mass, which can be compared to the $M_\bullet \sim 2 \times 10^7 M_\odot$ mass that was derived from the $M_\bullet - M_{\text{stars}}$ relation of Schutte et al. (2019) in Paper I. Turning first to the case of gravitationally-bound gas, the observed $\sim 600 \text{ km s}^{-1}$ velocity gradient implies an orbital speed of $v \approx 300 \text{ km s}^{-1}$ at $r \approx 1 \text{ kpc}$. The implied mass is

$$M_\bullet \approx \frac{v^2 r}{G} \approx 2 \times 10^{10} M_\odot, \quad (\text{A1})$$

higher by three orders of magnitude than expected from the stellar mass of the galaxy.

One could also imagine that the gradient arises from hyperbolic encounters of the SMBH with ambient gas, as explored by Ogiya & Nagai (2024). In the Ogiya & Nagai impulsive limit, the parallel kick at impact parameter b is

$$\Delta v_{\parallel} \approx \frac{2G^2 M_\bullet^2}{V^3 b^2}. \quad (\text{A2})$$

Conservatively interpreting the observed $\sim 600 \text{ km s}^{-1}$ gradient as a symmetric two-sided shear gives $M_\bullet \approx 1 \times 10^{11} M_\odot$ for $\Delta v_{\parallel} \approx 300 \text{ km s}^{-1}$, $b \approx 1 \text{ kpc}$, and $V \approx 1000 \text{ km s}^{-1}$.

We infer that in either interpretation an implausibly massive SMBH is required, and therefore reject a purely gravitational origin (bound or impulsive) for the gradient.

B. SENSITIVITY OF THE KINEMATICS FIT TO MODEL PARAMETERS

B.1. Effect of Parameter Variations

In § 4.4 we modeled the velocity flows across the bow shock to constrain the black hole velocity v_\bullet , the inclination i , and the radius of the cross section R_{ring} . In Fig. 12 we show the effects of varying the fit parameters. The black hole velocity, shown at left, is effectively a scaling of the entire curve. The inclination has a qualitatively different effect, as it impacts the ratio between the amplitude of the gradient ($\propto \cos i$) and the plateau velocity ($\propto \sin i$). The black hole velocity and the inclination can therefore be inferred from the observed velocity curve (see below).

The right panel of Fig. 12 shows the effect of changing the “fixed” parameters χ ($2.5 \leq \chi \leq 3.5$), θ ($30^\circ \leq \theta \leq 60^\circ$), and p ($0.5 \leq p \leq 2$). The impact on the velocity profiles is small compared to that of the black hole velocity and the inclination.

B.2. A Simple Method to Estimate the Black Hole Velocity and Inclination

Here we point out that v_\bullet and i can also be estimated directly from the data. Assuming that the amplitude of the gradient $A = (v_{\text{max}} - v_{\text{min}})/2$ and the absolute plateau velocity B have been measured, and ignoring the azimuthal and disk/ring factors in Eq. 8, the inclination can be inferred from B/A :

$$i \approx \arctan \left[\frac{\sin 2\theta}{2(1 - 1/\chi)} \frac{B}{A} \right]. \quad (\text{B3})$$

For $\theta \approx 60^\circ$ and $\chi \approx 3$ this reduces to

$$i \approx \arctan \left(0.65 \frac{B}{A} \right). \quad (\text{B4})$$

The black hole velocity follows from the inclination and the plateau velocity:

$$v_\bullet = \frac{\chi}{\chi - 1} \frac{B}{\sin i} \approx \frac{3}{2} \frac{B}{\sin i} \quad (\text{B5})$$

for $\chi \approx 3$. Applied to our data, we have $A \approx 317 \text{ km s}^{-1}$, $B \approx 313 \text{ km s}^{-1}$, and therefore $i \approx 33^\circ$ and $v_\bullet \approx 860 \text{ km s}^{-1}$. These values are only $\sim 10\%$ removed from the results of the full model fit.

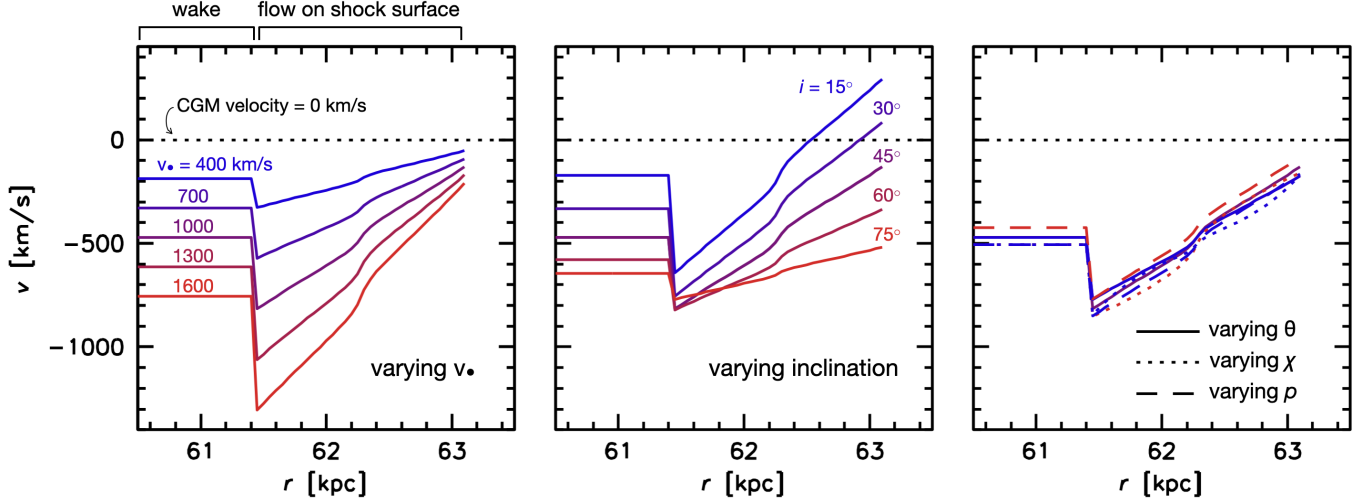


Figure 12. Dependence of the velocity profile on the parameters of the model. The default model here has black hole velocity $v_{\bullet} = 1000 \text{ km s}^{-1}$, inclination $i = 45^\circ$, obliquity $\theta = 60^\circ$, compression factor $\chi = 3$, and disk/ring parameter $p = 1$. *Left:* Effect of varying v_{\bullet} . *Middle:* Effect of varying the inclination. *Right:* Effect of varying $45^\circ \leq \theta \leq 70^\circ$, $2.5 \leq \chi \leq 3.5$, and $0.5 \leq p \leq 2$. The black hole mass and inclination are the dominant parameters, and they can be determined independently from the combination of the plateau velocity and the amplitude of the gradient.

C. VELOCITY DISPERSION MEASUREMENT FROM LRIS DATA

The analysis in Paper I was largely based on low resolution spectra obtained with the $400 \text{ lines mm}^{-1}$ grating, as these have the highest S/N ratio. However, we also obtained higher resolution observations with the $1200 \text{ lines mm}^{-1}$ grating. The spectral resolution (as measured from sky emission lines) is $\sigma_{\text{instr}} = 18 \text{ km s}^{-1}$. The 2D spectrum near the [O III] $\lambda 5007$ line is shown in Fig. 1 of paper I, and repeated in the inset of Fig. 13. The main panel of Fig. 13 shows the averaged spectrum of the [O III] knot at the tip. A Gaussian fit gives $\sigma_{\text{obs}} = 1.17 \pm 0.14 \text{ \AA}$, or $36 \pm 4 \text{ km s}^{-1}$. Correcting for the instrumental resolution gives $\sigma = 31 \pm 4 \text{ km s}^{-1}$ for the dispersion of the gas.

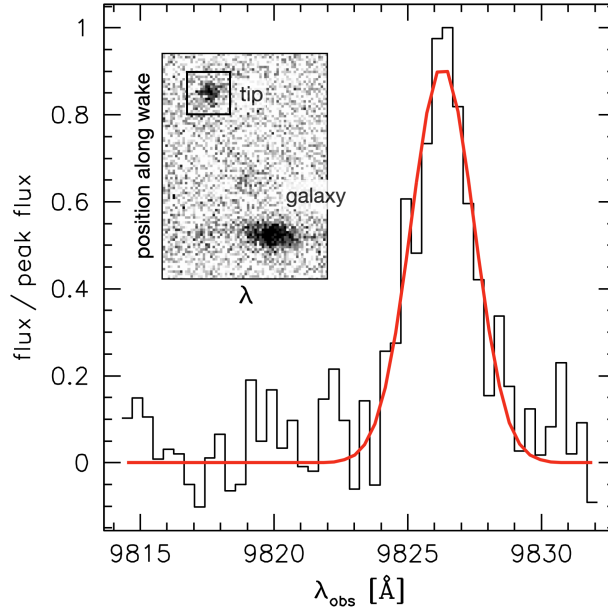


Figure 13. *Inset:* High resolution 2D Keck/LRIS spectrum of RBH-1 in the [O III] $\lambda 5007$ region, with $\sigma_{\text{instr}} = 18 \text{ km s}^{-1}$. These data were previously shown in Fig. 1 of Paper I. *Main panel:* Velocity profile of the knot at the tip of the wake, with the best-fitting Gaussian in red. The width of the line is $\sigma = 30 \pm 4 \text{ km s}^{-1}$ after correcting for instrumental resolution.

The dispersion is significantly higher than the thermal broadening: at $T \sim 10^4$ K the thermal dispersion is $\sigma_{\text{th}} \approx 2\text{--}3 \text{ km s}^{-1}$ for oxygen ions. The two components that are likely contributing to the dispersion are the $\sim 600 \text{ km s}^{-1}$ velocity gradient induced by the bow shock limbs and turbulence. Disentangling these components requires data of higher S/N ratio and spatial resolution.